Materials Science and Engineering, R13 (1994) 1–56

R Reports: *A Review Journal*

High resolution X-ray diffraction characterization of semiconductor structures

Chu Ryang Wie

Department of Electrical and Computer Engineering, State University of New York at Buffalo, 201 Bonner Hall, Buffalo, NY 14260, USA

Received 18 January 1994; accepted 11 April 1994

Abstract

The high-resolution X-ray diffraction techniques, such as double-crystal rocking curve and triple-crystal diffraction, have become essential tools in the semiconductor materials and devices laboratory. Quick and non-destructive characterization is possible for basic layer parameters including layer composition, strain, mismatch and thickness. More sophisticated characterization of interface and quantum-well structures with submonolayer resolution is possible with the help of kinematical diffraction principles and diffraction profile simulation using the dynamical diffraction theory. These X-ray diffraction techniques are making it possible to correlate the structural properties to the epitaxial growth processes, to the electrical/optical properties and to the device performance. In this review article, I discuss some basic aspects of the instrument, simple determination of layer parameters, the dynamical and kinematical diffraction theories, and some recent results in the characterization of heterostructure interfaces and strained quantum-well devices. I also discuss the diffuse scattering analysis of bulk semiconductors in the Bragg diffraction geometry. Interface analysis of the lattice-matched structures such as GaInAs/InP and AlGaAs/GaAs is discussed in terms of kinematical diffraction principles, namely the *X-ray phase shift* and the *crystal truncation rod*. Analysis of strained quantum wells is discussed using Bragg peak profile and Pendellösung fringe profile. Diffuse scattering in bulk semiconductors is discussed in the context of the analysis theory, namely the rocking-curve profile and the radial intensity profile around a reciprocal lattice point of the diffuse scattered X-rays due to such defects as dislocation loops and spherical defect clusters.

1. Introduction

With advances in the epitaxial growth techniques (such as molecular-beam epitaxy and metal-organic chemical vapor deposition and their variations) and due to the importance of knowing the structural characteristics of the epitaxial layers for application in high-performance electronic and optoelectronic integrated-circuits technology, the X-ray rocking-curve technique has quickly become a most essential and versatile tool for characterizing heteroepitaxial structures. The X-ray rocking-curve technique is relatively fast and non-destructive, and requires no particular sample preparation. Simple layer parameters such as layer thickness and composition (for a ternary layer) can be quickly obtained from the X-ray rocking-curve data. The structural information from the X-ray rocking-curve data is often complementary to the information obtained from transmission electron microscopy (TEM) data or from photoluminescence (PL) spectroscopy data. By combining the X-ray rocking-curve and photoluminescence characterizations (which are both non-destructive) with the electrical and device studies, or in other words, by correlating the growth, structural,

SSDI 0927-796X(94)00169-S

electrical/optical and device properties, one can perhaps try to optimize the growth process for the device structure of interest. The basic techniques of rocking-curve analysis have been reviewed previously [1–3].

X-Ray diffraction is very sensitive to the lattice strain. Lattice strains may be caused by lattice defects or heteroepitaxy. Point defects are too small to be observed by conventional imaging techniques in TEM, but they do have appreciable effects on the X-ray intensity profile. On the other hand, X-ray diffraction is insensitive to those lattice defects, often of sufficient size for detection by TEM, that do not deform the host lattice, such as incoherent precipitates. The strain fields produced by randomly distributed defects such as interstitials, point-defect aggregates, dislocations, thermal vibrations, etc., contribute to incoherent, diffuse scattering and cause a change in the average lattice parameter. For a given incident angle (or for a given incident wave vector), the diffuse-scattered X-ray intensity is distributed over a reciprocal-space volume of typically 10^{-3} Å$^{-1}\times10^{-3}$ Å$^{-1}\times10^{-3}$ Å^{-1}. This volume may be compared with a typical Bragg peak width, 6 arcsec or 2×10^{-5} Å^{-1}, of a perfect crystal. For the epitaxial alloy layers, the lattice strain contributes mostly to the coherent Bragg diffraction because the lattice strain in a heteroepitaxial layer is coherent. For strained epitaxial layers and for the interfaces of certain heterostructures, high-resolution X-ray diffraction (HRXRD) is capable of providing structural information on a submonolayer scale.

Under optimum conditions, X-ray diffraction is capable of detecting strains in single-crystal silicon of less than 10^{-8} [4]. In double-crystal X-ray diffraction (DCD), short-wavelength and high-order reflections in a non-dispersive (+ −) setting (i.e. identical crystals for the first crystal and for the sample crystal, which are arranged antiparallel to each other) are used in order to achieve such a high strain sensitivity. Changes in lattice spacing cause proportional changes in the Bragg angles for X-ray diffraction, as shown below [5]. The strain sensitivity depends upon the constant of proportionality and the minimum shift in Bragg angle which can be detected. This minimum detectable shift depends upon the width of the Bragg peak. Thin epitaxial layers have relatively broad Bragg peaks, and the strain sensitivity of the X-ray technique is reduced for thin layers. Crystal defects in the layer also broaden the Bragg peaks and further reduce the strain sensitivity. A strain sensitivity of about 10^{-5} is typical for crystal layers a few thousand ångströms thick when using a DCD (with a highly perfect first crystal), and sample Bragg angle near 45°. For samples where the substrate is not useful as a reference for Bragg peak shift, such as (001) silicon epi layer on a $(01\bar{1}2)$ sapphire substrate, an X-ray method to measure the strains was developed by Vreeland, who affixed a stress-free reference crystal to the surface of the strained film and measured the film strains relative to this reference [5].

In this review, I discuss some basic elements of the high-resolution diffraction technique, analysis methods for heteroepitaxial layers and their interfaces, and the analysis of diffuse scattering for defect characterization. This paper is organized as follows:

Section 1 a general introduction,

Section 2 fundamental elements of the technique,

Section 3 some basics needed in interpreting X-ray rocking curves for heteroepitaxial samples,

Section 4 dynamical and semi-kinematical diffraction theories and optical principles of kinematical X-ray diffraction,

Section 5 X-ray rocking-curve analysis of heterointerfaces, superlattices and strained quantum wells, and

Section 6 a brief review of theory and experiments of diffuse scattering for the characterization of defects in bulk semiconductors as studied by DCD and triple-crystal diffraction (TCD).

1.1. Lattice parameter change in bulk semiconductors from high-concentration impurities or point defects

The semiconductor device processing techniques for microelectronics and integrated circuits, such as ion implantation and thermal diffusion, produce various crystal defects such as substitutional, interstitial and vacancy-type point defects and dislocations. For crystals with dominantly substitutional defects (including vacancies), the defect concentration can be found from the lattice parameter measurement assuming a simple linear variation of the lattice constant with the defect concentration. For example, from a study of thermally diffused silicon crystal, a negative volume change of 5.00 ± 0.16 Å^3 per boron atom and 1.72 ± 0.15 Å^3 per phosphorus atom was found, from which the depth profile of impurity concentration was determined. It was shown that a boron or phosphorus impurity concentration greater than 10^{18} cm^{-3} produces a lattice strain observable with DCD [6]. This minimum concentration of impurity, for detection by DCD, corresponds to about 2×10^{-5} in atom fraction and to about 4×10^{-6} in the perpendicular lattice mismatch. In an isoelectronic doping experiment, such as In or Sb in GaAs [7], the DCD is an easy way to measure fractional atom concentrations of the order 10^{-3}. An analysis of boron-implanted silicon crystals showed a positive volume change of about 1.1 Å^3 per about ten Frenkel pairs (per boron ion), which amounts to about one-half of the Si atomic volume [8]. In samples involving both vacancies and interstitials, the average lattice spacing will change less sensitively with the defect concentration. In the rocking-curve analysis of bulk crystals with a high concentration of crystal defects, a careful analysis of the effect of diffuse scattering on the rocking-curve profile may be also needed as, for example, in Ref. [9]. The diffuse-scattering analysis is the subject of Sections 1.3 and 6.

1.2. Interface structure of lattice-matched heterostructures

We shall discuss the analysis of interface structures in lattice-matched heterostructures such as GaInAs/InP, GaInP/GaAs, AlGaAs/GaAs, etc. The HRXRD is capable of providing information on the interface structure with monolayer (ML) resolution. X-Ray diffraction is due to the interference of the X-ray waves reflected by atomic planes. If a portion of the crystal lattice has a slightly different lattice spacing, then a relative phase shift proportional to $t\epsilon_f$ [10,11] occurs in the diffracted wave where t is the thickness of the strained portion of crystal and ϵ_f is the mismatch or the fractional difference in the lattice parameter. A large lattice mismatch thus requires only a small thickness for the same relative phase shift. For example, if an $Al_{0.3}Ga_{0.7}As$ layer 1000 Å thick replaces a certain portion of a GaAs crystal ($\epsilon_f = 3.9 \times 10^{-4}$), then the X-ray wave diffracted by the GaAs crystal which lies below the AlGaAs layer will have an additional phase delay proportional to 1000 (3.9×10^{-4}) Å compared with the wave diffracted by GaAs which lies above the AlGaAs layer. Suppose that InAs instead of $Al_{0.3}Ga_{0.7}As$ has replaced GaAs in the same region. Then the same phase delay will occur over InAs only 5.62 Å thick, which is less than two monolayers in the [001] direction. In $Ga_{1-x}In_xAs/InP(001)$, the interface must have at least one molecular layer of $Ga_{1-x}In_xP$ or InAs. A large lattice mismatch of these interfacial molecular layers

with respect to the surrounding crystals makes the X-ray rocking-curve profile very sensitive to a detailed interface structure.

The following relationship of lattice parameters among different crystals is useful in the interface analysis by HRXRD: (Si, GaP, AlP, ZnS) $+3.7\% \rightarrow$ (Ge, GaAs, AlAs, $Ga_{0.5}In_{0.5}P$, ZnSe) $+3.8\% \rightarrow$ (InP, $Ga_{0.5}In_{0.5}As$, CdS) $+3.6\% \rightarrow$ (InAs, GaSb, AlSb, ZnTe) $+6.6\% \rightarrow$ (InSb, CdTe), where the materials within each pair of parentheses have a relatively small lattice mismatch with each other (less than 6×10^{-3}), and the lattice parameter increases by the given percentage moving to the right. A lattice-matched heteroepitaxy of $Ga_{0.5}In_{0.5}P$ on GaAs(001) will have a highly strained molecular layer of GaP or $Ga_{0.5}In_{0.5}As$ ($\pm3.7\%$ mismatch) in the interface, which was considered in the analysis of the experimental rocking curve in Ref. [12]. A heterostructure or superlattice of InAs/GaSb with only a 0.6% lattice mismatch between the layers of the sample will have as highly strained interfacial molecular layers as InSb and GaAs with an almost $\pm7\%$ mismatch. Another interesting example is the InSb/CdTe [13] and GaAs/ZnSe [14] superlattices, with a close lattice match between the layers, but with an unknown interfacial layer. High-resolution X-ray diffraction is well suited for the interface study of such heterostructures.

A similar argument indicates that the XRD profile is not very sensitive to the interface structure of such lattice-matched structures as AlGaAs/GaAs and AlInP/GaInP (on a GaAs substrate), and AlInAs/GaInAs (on an InP substrate), because no such highly strained interfacial molecular planes exist. In this case, the interface analysis by X-ray rocking curves is done not using the strain-dependent phase shift but using the effect that the crystal truncation at the interface has on the diffraction profile. Here, the crystal truncation at the interface is meant to indicate the discontinuity in layer composition and in layer strain, but not any discontinuity in the crystal lattice. This is different from the crystal truncation at the sample surface, where the crystal lattice itself is terminated.

1.3. Diffuse X-ray scattering analysis of defects in semiconductors

The local lattice structure around every crystal defect is distorted. The X-ray diffraction technique probes a crystal volume of, say, $1\ \text{mm}\times1\ \text{mm}\times10\ \mu\text{m}$. Thus a collective consequence of the lattice distortion by many defects can be seen as a broad, low-intensity profile centered near the Bragg peak (or near a reciprocal lattice point) in the X-ray diffraction data. Anisotropy (or isotropy) of the distribution of the diffuse-scattered X-ray intensity in the reciprocal space is a characteristic of the kind of defects involved. For defects such as clusters of point defects and dislocation loops with a size greater than about 15 Å in radius, HRXRD (DCD and TCD) measurement and analysis of the data can be used to find structural information such as defect type, size, concentration, and the scattering strength. For a high concentration of defects of smaller sizes, single-crystal diffraction (SCD) can be used for the diffuse-scattering analysis [15].

Much theoretical work is now available for analyzing the data in uniform bulk-crystal samples [16–21]. For layered semiconductor structures, experimental data are interpreted qualitatively [22,23] because no practical analysis theory is available for diffuse scattering in these structures. Since the TCD technique is capable of measuring a two-dimensional (2-D) distribution of the scattered X-ray intensity in the reciprocal space, this technique (and DCD to a limited extent) is naturally suited for the diffuse-scattering analysis of crystal defects. Many TCD and/or DCD studies of the defects in bulk semiconductors Si, GaAs and InP have been reported in the literature. More recently, TCD studies of semiconductor

heterostructures and II–VI compounds have been conducted. In Section 6, I try to provide an overview of some of the published diffuse-scattering data for bulk semiconductors, organized according to the types of TCD/DCD data: the TCD isointensity contour data (the distribution of scattered intensity in a 2-D reciprocal plane), the TCD profile data, and the DCD profile data.

2. Elements of high-resolution X-ray diffraction

HRXRD gives a Fourier transform of a crystal volume of typically 1 mm×1mm×(5−50) μm. The data are the X-ray intensity distributed in the vicinity of a reciprocal lattice point (or a Bragg peak). The typical wave-vector resolution is about 10^{-5} Å^{-1}, obtained over an approximate range up to 10^{-4}–5×10^{-3} Å^{-1} around the reciprocal lattice point. Fig. 1 shows schematics of typical HRXRD systems. The plane of this figure coincides with the *diffraction plane* defined by the incident ($\mathbf{k}_0$) and diffracted ($\mathbf{k}$) wave-vectors. (Throughout this paper, the lower-case letter **k** refers to the wave-vector inside the crystal medium and the upper-case letter **K** for outside the crystal.) In both DCD and TCD, the measured intensity is an integrated intensity, integrated over the (vertical) direction normal to the diffraction plane by a detector wide-open in that direction. TCD can provide either a 2-D distribution of the scattered intensity, distributed in the diffraction plane, or a profile along a particular direction in the diffraction plane. DCD provides the data as the scattered intensity integrated over a wide range of scattering angle, the integrated intensity given as a function of the incident angle (it is the so-called double-crystal X-ray rocking curve because the incident angle is varied by 'rocking' the sample). Below, there will be a brief discussion on monochromating (single-wavelength X-ray) and collimating (i.e. making a plane wave of) the incident beam. Schematics of some of the more-often-used monochro-collimators (MC) and analyzer crystals (AC) are illustrated in Fig. 2. I shall also discuss in this section two kinematical diffraction principles and how the TCD/DCD data are presented.

2.1. Beam monochromation and collimation

A high angular resolution, and thus a high strain sensitivity, is achieved by monochromating and/or collimating the incident X-ray beam. It is accomplished by reflecting the incident beam off a high-quality single crystal once or several times before the beam is incident onto the sample crystal. The collimation process can be understood by considering a calculated rocking-curve profile for a single bulk crystal. Fig. 3 shows semilog plots of the calculated X-ray rocking curves for perfect Si(220) and GaAs(004) crystals. The calculation was done

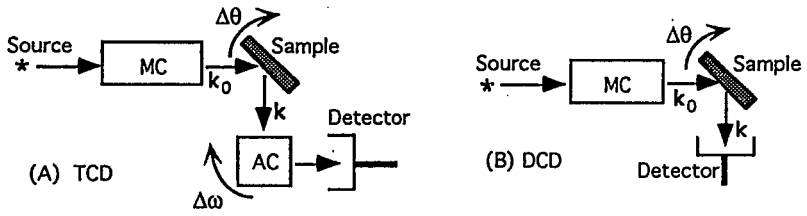

Fig. 1. Schematics of HRXRD systems: (A) triple-crystal diffractometer, (B) double-crystal diffractometer. The monochro-collimator (MC) and analyzer crystals (AC) are shown in Fig. 2.

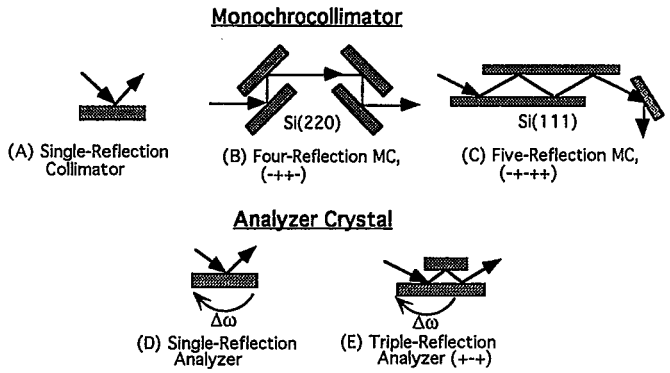

Fig. 2. Schematic illustrations of monochrocollimator and analyzer crystals. (A) single-reflection collimator; (B) four-reflection MC $(-++-)$; (C) five-reflection MC $(-+-++)$; (D) single-reflection analyzer; (E) triple-reflection analyzer $(+-+)$. Two U-grooved crystals in (B) and one U-grooved crystal in (C) and (E) could be used.

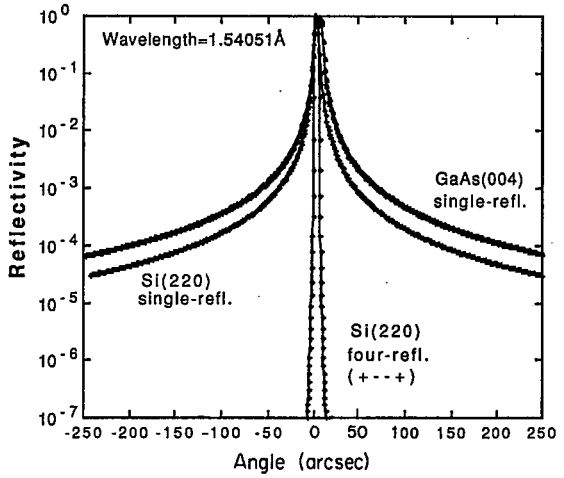

Fig. 3. Calculated Bragg reflection profiles (i.e. rocking curves) for beam-conditioning crystals, Si(220) and GaAs(004). The long Bragg tail present in a single reflection is eliminated by a multiple reflection such as $(+--+)$.

assuming a completely collimated (i.e. plane-wave) monochromatic incident beam. Fig. 3 shows the reflectivity as a function of the grazing angle of incidence. Suppose now that a monochromatic, but angularly divergent, beam was used as the incident beam. This beam is incident onto a crystal (the MC crystal), which is fixed in position and does not rotate. The intensity angular profile of the reflected beam as a function of direction of the reflected wave vector **K** (or the exit angle) should be the same as the single-reflection curve in Fig. 3. In other words, for X-rays incident at angles belonging outside the Bragg profile, their intensities after reflection will be much reduced, to the tail level of the profile.

Therefore, after a single reflection an angularly diverging X-ray beam at a given wavelength (λ), emerging from the X-ray source, will be collimated approximately to within the rocking-curve width (typically about 5 arcsec), but with a rather broad tail which varies from about 10^{-1} to 10^{-5} in reflectivity for angles deviating from the Bragg angle. Reflecting more than once from the crystal faces fixed in space will drastically reduce the tail of the intensity profile of the emerging X-ray beam. This is illustrated in Fig. 3 for a four-reflection Si(220) MC crystal where, for example, a reflectivity of 10^{-2} by a simple reflection becomes 10^{-8} by four reflections. A MC crystal therefore acts as an extremely narrow 'slit'. It

produces an essentially plane wave for each wavelength component. For example, for the Cu $K\alpha_1$ and Cu $K\alpha_2$ characteristic lines listed in Table 1 which emerge from the X-ray source in a spherically diverging manner, a single 004 reflection from a GaAs crystal will produce two (nearly) plane waves with their propagation directions separated by about 333 arcsec. Therefore, a finite range of different X-ray wavelengths (the pass-band) will be found in the outgoing beam from MC.

Monochromation occurs when the X-ray reflects off two successive, fixed crystal faces arranged such that the scalar product of their surface normals yields a positive number (such as the second and third reflections in Fig. 2B and the fourth and fifth reflections in Fig. 2C). In the literature, this is called the dispersive arrangement or the dispersive $(+\,+)$ or $(-\,-)$ setting, where the signs refer to the relative sense of the surface normal vectors, with respect to each other, of the two successive crystal faces (see also Fig. 2). Key to the monochromation by a $(+\,+)$ or $(-\,-)$ setting lies in the fact that the *X-ray emerging from the first face at a larger glancing angle enters the second face at a smaller glancing angle.* Remember the Bragg law that a longer-wavelength X-ray needs a larger entrance angle for the Bragg reflection. Let us consider two wavelengths $\lambda_1 > \lambda_2$. If λ_1 is strongly reflected from a given $(+\,+)$ setting, then λ_2 will be eliminated. This is because even if λ_2 is strongly reflected from the first face, the entrance angle of λ_2 to the second face will be larger than that of λ_1 (but λ_2 needs a smaller angle than λ_1 because $\lambda_1 > \lambda_2$). Therefore, in a multiple-reflection MC, at least two successive reflections must be arranged in a $(+\,+)$ or $(-\,-)$ dispersive mode (such as between the second and third reflections in Fig. 2B). This makes the λ spread in the outgoing beam from MC typically less than 10^{-4} Å, essentially monochromatic.

A MC assembly for an extremely narrow λ- and θ-spread was described in Ref. [25] where a three-reflection $(+\,+\,-)$ Si(001) MC crystal, with two extremely asymmetric 422 reflections ($2\theta_B = 88°$) of Cu $K\alpha_1$ X-ray, is used to produce a θ- and λ-spread of 1.0 arcsec and 7.7×10^{-6} Å, respectively (the θ- and λ-spread for a given MC can be conveniently calculated using the diagram designed by DuMond, reported in Ref. [26]). In this MC, the second and third reflections were from a U-grooved monolithic Si crystal with a small-angle incidence for the second reflection and a large-angle incidence for the third reflection. Recently, the construction of a compact four-reflection $(+\,-\,-\,+)$ MC assembly using two U-grooved Si(220) crystals was described by Matyi [27].

In a $(+\,-)$ setting of two identical crystals, the two crystal faces being exactly parallel (anti-parallel rather) to each other, different wavelengths can be simultaneously Bragg-

Table 1
Selected wavelengths and relative intensities of commonly used target materials. Z (the first column) is the atomic number of the target material. Data from ref. [24]

Z	Target	Wavelength (Å)			Relative intensity	
		$K\alpha_1$	$K\alpha_2$	$K\beta_1$	$I\alpha2/I\alpha1$	$I\beta1/I\alpha1$
24	Cr	2.28962	2.29351	2.08480	0.515	0.179
26	Fe	1.93597	1.93991	1.75653	0.500	0.167
27	Co	1.78892	1.79278	1.62075	0.497	0.160
28	Ni	1.65784	1.66169	1.50010	0.495	0.187
29	Cu	1.54051	1.54433	1.39217	0.497	0.200
42	Mo	0.70926	0.71354	0.63225	0.499	0.279
47	Ag	0.55936	0.56378	0.49701	0.499	0.290

reflected from both crystals. Here, for each wavelength, the emerging X-ray after the second reflection is exactly parallel to the X-ray incident to the first crystal. Therefore, this arrangement is called a non-dispersive setting. This arrangement can be found in a U-grooved crystal. In the case of double-crystal diffraction employing a single-reflection collimator, the sample crystal must be identical to the first crystal (the collimator) and these two crystals must be arranged in a $(+-)$ non-dispersive geometry so that the angular divergence due to different spectral components in the X-ray source may not contribute to the rocking-curve broadening. However, when a multiple-reflection monochro-collimator is used as the first crystal, then the sample crystal need not be identical, nor parallel, to the first crystal, because here only one wavelength is incident to the sample.

2.2. *Crystal truncation rods and X-ray phase shift*

Here, I should like to discuss briefly two important diffraction principles which will be used later for characterizing the interfaces of semiconductor heterostructures: (i) the effect of crystal truncation at the surface on the diffraction profile, and (ii) phase shift in the X-ray wave caused by lattice strain.

First, the crystal truncation effect: the X-ray rocking curve (the single-reflection curves in Fig. 3) of a bulk single crystal shows a rather long tail. This Bragg tail (also called the extended Bragg scattering) decreases roughly as $(\Delta\theta)^{-2}$, as indicated in Fig. 4. It represents a substantial intensity (of order 10^{-4} in reflectivity at $\theta_B \pm 200$ arcsec) and is due to termination of the crystal lattice at the surface.

X-ray diffraction in Bragg geometry from a bulk crystal corresponds to Fourier-transforming a semi-infinite crystal lattice (semi-infinite in one dimension owing to the truncation of the crystal at surface, and infinite in the other two dimensions). The Fourier transform of a step function, representing the crystal lattice in the surface normal direction, is $1/q$ where q corresponds to the wave-vector difference of the diffracted X-ray between air and crystal media. This wave-vector difference is proportional to the difference in refractive indices of the diffracted X-ray (unity in air and $1-\delta$ in crystal). The refractive index of the crystal, $1-\delta$, depends on the incidence angle through the dispersion equation

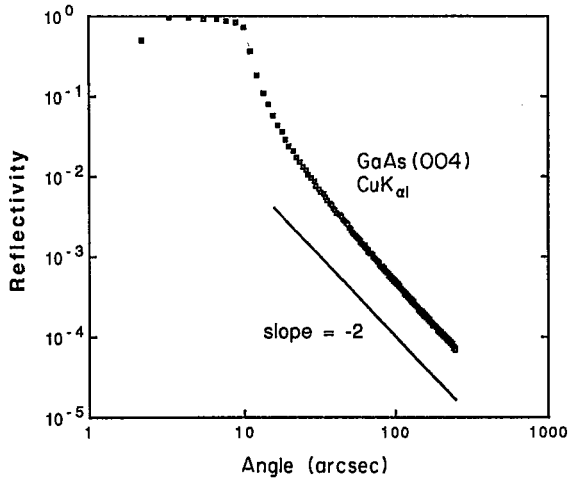

Fig. 4. Log–log plot of the GaAs(004) Bragg reflection profile using Cu $K\alpha_1$. Note that the Bragg tail, caused by the abrupt termination of the crystal lattice at the surface, decreases as $(\Delta\theta)^{-2}$.

(dynamical diffraction, see Ref. [28]). Approximately, δ (and thus q) is proportional to $\Delta\theta$, the deviation of incident angle from the Bragg angle. Or, more simply put, q is the deviation from the reciprocal lattice point in the reciprocal space. The diffraction intensity (square of the Fourier transform) has then a q^{-2} or $(\Delta\theta)^{-2}$ dependence near each of the Bragg points. If the surface of the bulk crystal is very rough (so that the transition from crystal to air is very gradual), Robinson [29] has shown that the tail of Bragg profile decreases as $(\Delta\theta)^{-4}$. This can be qualitatively understood from the fact that the Fourier transform of a broadened step function decays in the reciprocal space much faster than $1/q$. In the distribution of scattered intensity in a three-dimensional reciprocal space, this Bragg tail appears as an elongated 'rod' or 'streak' aligned in direction normal to the crystal surface. It is called the *crystal truncation rod* (CTR) [29]. Note that the boundary condition at the crystal surface requires matching the surface-parallel components of the wave-vectors between the interior and exterior of the crystal.

Thus a continuum of scattered wave-vectors (corresponding to CTR) is possible only along the surface-normal direction. This continuum of momentum transfer to the diffracted X-ray photons is caused by a single layer of atoms at the crystal surface [29]. For a thin layer on a substrate, there are two step functions present, one for the interface and one for the surface. The more gradual interface (or surface) of the two may determine the CTR profile of the thin layer (this needs more careful analysis). Note that the CTR is a coherent diffuse scattering, in contrast with the (mostly incoherent) diffuse scattering caused by randomly distributed defects.

Second, the phase shift of the X-ray wave caused by the lattice strain: consider lattice planes with spacing d. Each lattice plane partially reflects and partially transmits the X-ray. For a monochromatic plane-wave incident beam of wavelength λ incident at a glancing angle θ, the phase difference between the X-rays reflected by two successive lattice planes is $(2\pi/\lambda)2d \sin\theta$. Suppose that the lattice spacing has increased by Δd. Then, the phase difference will increase by $(2\pi/\lambda)2\Delta d \sin\theta = (2\pi/\lambda)2\epsilon d \sin\theta$, where $\epsilon = \Delta d/d$. Now consider the phase difference between the X-rays reflected by two lattice planes between which n lattice planes with a total thickness t $(=nd)$ are inserted. The phase difference is $(2\pi/\lambda)2t \sin\theta$ between the two lattice planes under consideration. If the lattice spacing in the inserted material increases by Δd then the phase difference will increase by $(2\pi/\lambda)2n\,\Delta d \sin\theta = (2\pi/\lambda)2\epsilon t \sin\theta$. The lattice strain in the inserted material can therefore affect the X-ray interference profile. Highly strained interfacial layers (a perpendicular strain of 7% is a common value) or a strained (single or multiple) quantum-well layer can be studied by analyzing the X-ray rocking-curve profile.

2.3. Resolution and description of TCD/DCD data

HRXRD measures, with high resolution in angle and thus in the scattering vector, the intensity of scattered X-rays distributed in the neighborhood of a reciprocal lattice point (or a Bragg peak). The reciprocal lattice point therefore serves as the reference position (origin of the coordinates) in the reciprocal space in describing the distribution of scattered intensity. The scattered intensity is described as a function of deviation ($\mathbf{q}$) of the scattered wave-vector ($\mathbf{K}$) from the reciprocal lattice point. (This vector $\mathbf{q}$ equals the scattering vector, $\mathbf{K}-\mathbf{K}_0$, minus the reciprocal lattice vector $\mathbf{h}$.) In the case of a multilayer structure, the substrate Bragg peak serves as reference. In both TCD and DCD, the $\mathbf{q}$-vector lies within the diffraction plane because the scattered intensities distributed in direction normal to

the diffraction plane (the vertical direction) are integrated by a wide-open detector. (The monochromator and analyzer crystals resolve different wave-vectors only within the diffraction plane.) The vertical acceptance angle of the detector could be as large as $\pm 5°$, given by the detector area and its distance from the sample if no vertical slit is placed in between. A vertical slit of 1 mm in height and 10 cm in distance from the sample will give a vertical acceptance angle of 0.57°. The vertical integration of scattered intensity has an important implication on the q-dependence of the diffuse intensity profile of X-rays scattered by crystal defects. This will be further discussed in Section 6.

In TCD, the diffracted intensity is measured as a function of two angles: incidence angle to the sample crystal ($\Delta\theta = \theta - \theta_B$, where θ is the grazing angle of incidence and θ_B is the Bragg angle) and scattering angle from the sample crystal ($\Delta\omega = \omega - 2\theta_B$ where ω is the scattering angle). Conversion of these angular variables to the **q**-coordinate axes, which all lie within the diffraction plane, is done as follows:

$$\begin{aligned}(q_1, q_2) &= K(\Delta\omega \cos\theta_B, (2\Delta\theta - \Delta\omega)\sin\theta_B),\\ (q_E, q_0) &= K(\Delta\omega, \Delta\theta \sin(2\theta_B)), \text{ and}\\ (q_z, q_x) &= (q_1 \cos\phi + q_2 \sin\phi, -q_1 \sin\phi + q_2 \cos\phi)\end{aligned} \tag{1}$$

where only one axis of the axes pair needs definition: q_1 is parallel to the reciprocal lattice vector **h**, q_E is parallel to the Ewald sphere which is defined below, and q_z is parallel to the outward surface normal of the sample crystal. Here, $K = 1/\lambda$ and ϕ is the angle between sample surface and lattice plane. The (q_1, q_2) coordinate system is most frequently used in presenting the TCD data, usually in the form of isointensity contours. For a symmetric reflection ($\phi = 0°$), the two coordinate systems, (q_1, q_2) and (q_z, q_x), coincide. Fig. 5 shows a calculated isointensity contour plot from a (+ − +) triple-crystal diffraction, with a single-reflection collimator and a single-reflection analyzer. The scan modes of sample ($\Delta\theta$-scan) and analyzer ($\Delta\omega$-scan) which produce the crystal truncation rods are indicated in the

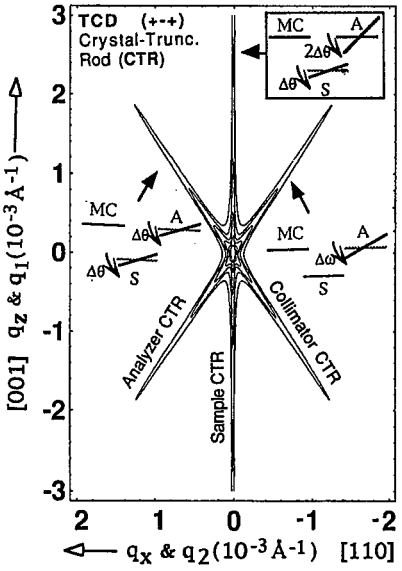

Fig. 5. Calculated isointensity contour plot for a (+ − +) TCD. The collimator, sample and analyzer were all GaAs(001) with 004 Cu Kα reflection. The crystal truncation rods (the long streaks) correspond to the long tails in a single reflection curve of Fig. 3. The TCD scan modes that produce each CTR are also indicated.

figure. The collimator CTR can be eliminated from the data by a multiple-reflection MC, and the analyzer CTR by a multiple-reflection analyzer, as suggested by the four-reflection profile in Fig. 3. The TCD data are sometimes presented as an intensity profile along a certain radial direction in the diffraction plane. Fig. 6 shows that the radial intensity distribution along a radial direction **q** in the diffraction plane, which makes an angle ψ with the q_2 axis, can be obtained in the TCD measurement by a combined scan of sample and analyzer:

$$\Delta\omega = 2\Delta\theta/(1+\cot\theta_B \cot\psi) \quad (2)$$

Elastically scattered X-rays outside the crystal satisfy the condition, $|\mathbf{K}| = 1/\lambda$ where **K** is the diffracted wave vector outside the crystal. This condition specifies a sphere in the reciprocal space, so called *Ewald sphere*. Fig. 7 shows an intersection of the diffraction plane with the Ewald sphere. In this figure, the incident angle θ is greater than θ_B. At $\theta = \theta_B$, the Ewald sphere passes through the reciprocal lattice point H (origin of the q coordinates) and at $\omega = 2\theta_B$ the scattered wave vector **K** falls on the point H. In Fig. 7, (*hkl*) is the reflecting lattice plane. A given incidence angle θ corresponds to a given Ewald sphere in the diffraction plane. At a given θ, all the scattered X-rays are distributed on the given Ewald sphere. In DCD measurement with a wide-open detector, all the scattered X-rays on the Ewald sphere (at the given θ) are integrated by the detector. When the double-crystal rocking curve is plotted against q, instead of against the incidence angle $\Delta\theta$, the q_0 coordinate is this q. Note that q_0, which is parallel to the scattered wave vector **K**, is the closest distance between the Ewald sphere and the origin (i.e., H).

In summary, Fig. 8 gives an illustration of all the q-coordinate systems, defined in Eq. (1), and an Ewald sphere at a given incidence angle and also the real space coordinate axes on the sample surface. Here, q_y axis (not indicated in the figure) and y axis are perpendicular to the diffraction plane. Since the X-ray beam usually travels horizontally and the diffraction plane is a horizontal plane, the q_y and y axes are sometimes called the vertical axis. Note also that at a given incidence angle θ (or $\theta - \phi$), the scattered wave vector **K** with a scattering angle $\omega = 2\theta_B$ ends at the intersection between the Ewald sphere and the q_2 axis, at a distance $2K \sin\theta_B \Delta\theta$ from the reciprocal lattice point H. This was shown in Fig. 7.

Different Ewald spheres can be resolved in the q space with a resolution of typically 10^{-5} Å^{-1} corresponding to a resolution of 3 arcsec in angle θ by the monochro-collimator. For example, for an AlGaAs/GaAs(001) heteroepitaxial sample studied by TCD near the

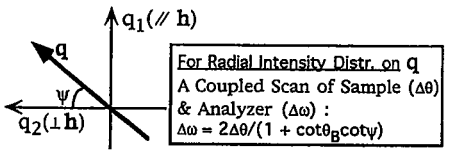

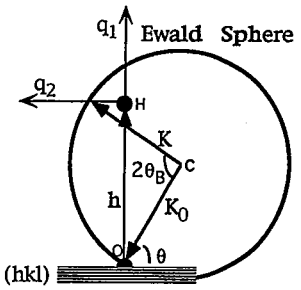

Fig. 6. Radial intensity distribution of scattered X-rays along a **q**-vector direction can be obtained by a combined scan of sample and analyzer in a TCD measurement.

Fig. 7. Ewald sphere for the description of Bragg scattered X-ray intensity. For a scattered angle $\omega = 2\theta_B$, the scattered wave vector coincides with the intersection of the Ewald sphere with the q_2 axis.

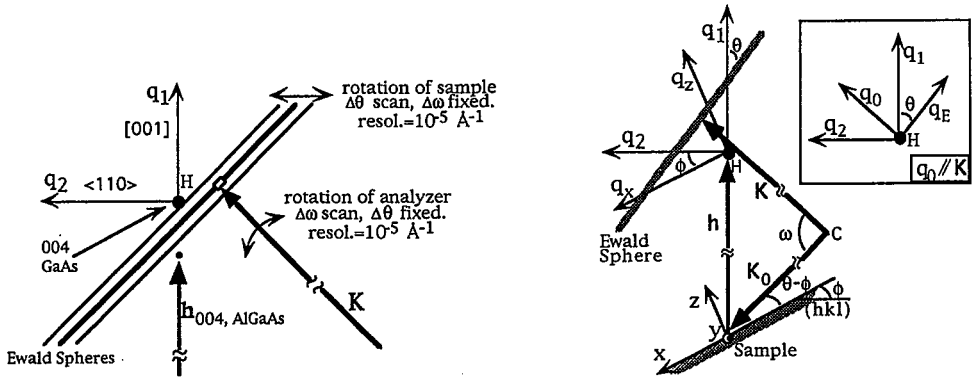

Fig. 8. Three coordinate systems in the diffraction plane of q space are defined. The (q_1, q_2) is relative to the reciprocal vector $\mathbf{h}$, (q_z, q_x) is relative to the sample surface, and (q_E, q_0) is relative to the Ewald sphere. Note that the q_y axis is perpendicular to this diffraction plane.

Fig. 9. TCD resolution of q vector, illustrated for 004 reflection in AlGaAs/GaAs(001).

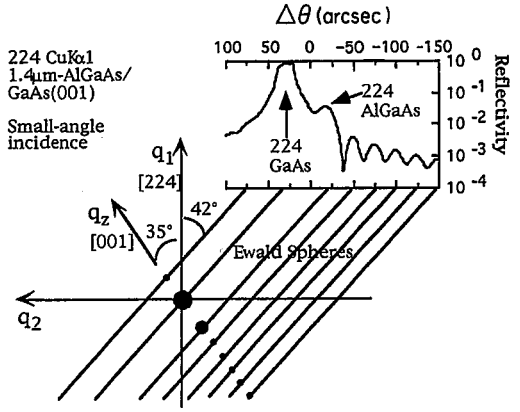

Fig. 10. Correspondence between the DCD rocking curve and the TCD reciprocal space map, illustrated for a 224 Cu $K\alpha_1$ reflection from 1.4 μm AlGaAs/GaAs(001). For clarity, only the Bragg and fringe peaks are drawn in the q space. Not drawn are the TCD isointensity contours.

004 reciprocal lattice point using Cu $K\alpha_1$, Fig. 9 illustrates a typical q-vector resolution. A different Ewald sphere corresponding to a different incidence angle θ can be resolved with a typical resolution of (3 arcsec)$|\mathbf{h}| = 10^{-5}$ Å^{-1}, assuming that the FWHM of the MC Bragg profile is 3 arcsec. The X-ray intensity distributed on an Ewald sphere is resolved with a typical resolution of (3 arcsec)$K = 0.9 \times 10^{-5}$ Å^{-1} by the analyzer crystal having a 3 arcsec rocking-curve width.

Fig. 10 shows the correspondence between the TCD **q**-plane distribution near the 224 reciprocal point and the 224 DCD rocking curve for an AlGaAs/GaAs(001) sample. This figure shows also that the Pendellösung fringe (thickness fringe) peaks of the AlGaAs layer are aligned along the surface-normal direction in the **q**-space and they appear as the periodic secondary peaks in the DCD rocking curve. As has been mentioned earlier, all the scattered intensity distributed on an Ewald sphere is integrated in DCD by the detector wide open in the direction of the Ewald sphere. Any (random) defect strain fields distributed along the wavefront of the scattered wave (real space) will produce incoherent diffuse scattering whose intensity is distributed along the Ewald sphere (reciprocal space), and its integral

sum is added to the DCD rocking-curve intensity at a given $\Delta\theta$. This can further broaden the rocking-curve peaks and reduce the signal-to-noise ratio.

3. Simple interpretation of double-crystal rocking curves

In this section I shall discuss the interpretation of the angular separation $\Delta\theta$ between the layer and substrate Bragg peaks in an X-ray rocking curve. I also discuss briefly the rocking-curve full width at half maximum (FWHM), structure factor, X-ray penetration depth, and the rocking-curve analysis of strain relief. In Section 4.4 a discussion is given on some simple optical principles (such as optical Fraunhofer diffraction) which can assist in the analysis of the X-ray rocking curves of a heteroepitaxial layer, a quantum-well structure, superlattices, and their interfaces.

3.1. Peak separation $\Delta\theta$

The commonest application of the X-ray rocking-curve technique is the determination of layer composition, strain, and mismatch from the angular separation between the layer and substrate Bragg peaks. Layer quality is determined from the rocking-curve broadening, and, for a sample with a single heteroepitaxial layer, the layer thickness can be found from the Pendellösung fringe spacing. This can be applied to any epi layer thick enough to produce its own observable Bragg peak. For superlattices (SL) and multiple quantum wells (MQW), the period thickness can be found from the spacing of principal interference fringe peaks to be discussed in Section 4.4. In this section, I shall discuss the determination of composition, strain, mismatch, and misorientation.

Referring to Fig. 11, the angular separation between two Bragg peaks, $\Delta\theta$, is decided by three contributing factors: the difference in the lattice d spacing, $\Delta\theta_B$, the difference in the $[hkl]$ directions, $\Delta\phi$, and the difference in the surface orientations, Ω. Note that $\Delta\phi$ is zero when the epi layer is fully strain-relaxed ($\epsilon_\perp = \epsilon_\parallel$) or when the lattice plane is parallel to the sample surface ($\phi = 0$). The angle Ω comes from the fact that, during the initial epitaxy, the arriving atoms arrange themselves on the growth surface to minimize the free energy, which can lead to misorientation between the substrate surface and the epi layer surface. Its sign reverses when the directions of incident and diffracted wave vectors are

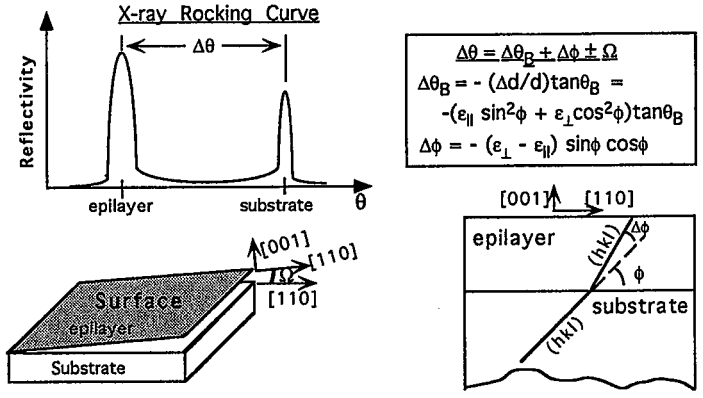

Fig. 11. The rocking-curve peak separation $\Delta\theta$ consists of three contributing factors. From measured $\Delta\theta$, the perpendicular ($\epsilon_\perp$) and parallel ($\epsilon_\parallel$) mismatches and the epi layer misorientation (Ω) can be obtained.

switched or by simply rotating the sample 180° around the surface normal. The perpendicular mismatch ($\epsilon_\perp$) can therefore be found from $\overline{\Delta\theta}$, an averaged $\Delta\theta$ from two symmetric ($\phi=0$) reflections, one with 0° and the other with 180° in azimuth, and the difference of these two equals 2Ω.

$$\epsilon_\perp = -\overline{\Delta\theta}\cot\theta_B \qquad \text{for symmetric reflection} \tag{3}$$

where $\overline{\Delta\theta}=0.5(\Delta\theta_{0°}+\Delta\theta_{180°})$. An average peak separation of two asymmetric ($\phi\neq 0$) reflections, such as 115, 224 or 333, gives the in-plane lattice mismatch ($\epsilon_\parallel$). Two asymmetric reflections with 90° and 270° in azimuth can give $\epsilon_\parallel$ along the other in-plane direction. Because the cleavage planes are {110}, the experimentally measured $\epsilon_\parallel$ is usually along ⟨110⟩, not along ⟨100⟩ as suggested in Fig. 12. Therefore, the elastic shear strain ϵ_{xy} equals $\epsilon_{\parallel,[110]}-\epsilon_{\parallel,[\bar{1}10]}$ and the compressive (or tensile) strain ϵ_{xx} equals $0.5(\epsilon_{\parallel,[110]}+\epsilon_{\parallel,[\bar{1}10]})-\epsilon_f$.

According to the linear elasticity theory, the perpendicular mismatch $\epsilon_\perp$ and the two in-plane mismatches, $\epsilon_{\parallel[\bar{1}10]}$ and $\epsilon_{\parallel[110]}$, are related to the misfit ϵ_f ($=(a-a_s)/a_s$) between the cubic cells of the bulk crystals.

$$\epsilon_f=[\nu\epsilon_{\parallel[110]}+\nu\epsilon_{\parallel[\bar{1}10]}+(1-\nu)\epsilon_\perp]/(1+\nu) \tag{4}$$

where ν is the Poisson ratio of the epi layer which equals $c_{12}/(c_{11}+c_{12})$ for (001) surface where c_{ij} is the elastic constant. The ternary-layer composition is found from ϵ_f through Vegard's law. It has been reported that the composition determined this way is more accurate than from analytical chemical techniques [30]. For lattice-matched layers and pseudomorphically strained layers for which $\epsilon_\parallel=0$, Eq. (4) holds accurately. However, the formula Eq. (4) has a significant error if used in (partially) strain-relaxed layers (i.e. $\epsilon_\parallel\neq 0$), as can be seen by the following test. A Poisson ratio ν was estimated from Eq. (4) using the X-ray measured $\epsilon_\perp$ and $\epsilon_\parallel$, and a known layer composition. The Poisson ratio thus estimated is listed in Table 2 using the X-ray and composition data in Ref. [31]. An increasing deviation of n from $c_{12}/(c_1+c_{12})\approx 1/3$ with the increasing $\epsilon_\parallel$ clearly indicates that Eq. (4) is not justified for the strain-relaxed layers. This may be due to the fact that Eq. (4) was derived by minimizing the elastic strain energy within the context of linear elasticity theory, while the strain-relaxed layers are systems with a (severe) plastic deformation. An increasing $\epsilon_\parallel$ means an increasing amount of plastic deformation in the layers.

For the pseudomorphic samples ($\epsilon_\parallel=0$) [32],

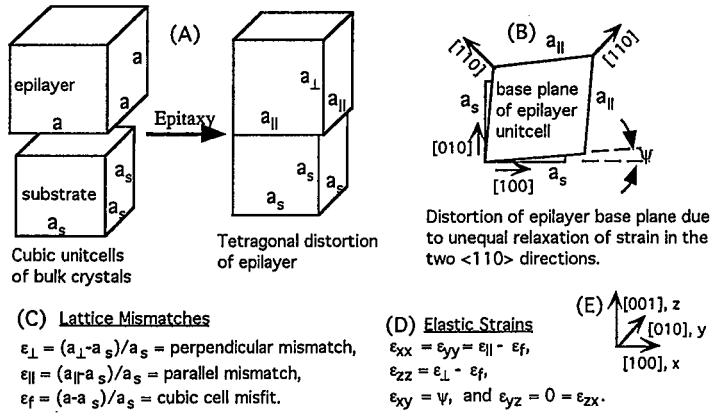

Fig. 12. Unit-cell distortion due to (A) heteroepitaxy and (B) strain relaxation. Definitions are given for (C) lattice mismatches, (D) elastic strains, and (E) coordinates.

Table 2
Apparent Poisson ratio ν estimated using Eqn. (4) from the X-ray data of ref. [31] for a partially strain-relaxed InGaAs layer 0.2 μm thick where x is the indium composition in InGaAs

x	0.05	0.08	0.12	0.15	0.20
$\epsilon_\perp$ (10^{-3})	6.58	9.94	10.6	13.1	16.8
$\epsilon_\parallel$ (10^{-3})	0.48	0.48	2.23	3.03	6.73
ν	0.32	0.27	0.15	0.13	0.14

Table 3
Elastic constants of semiconductor crystals (in 10^{11} dyn cm^{-2} or 10^{10} Pa)

Crystal	c_{11}	c_{12}	c_{44}	C	Ref.
Si	16.58	6.39	7.94	5.73	[32]
Ge	12.58	4.83	6.68	5.43	[32]
AlP	13.2	6.30	6.15	5.40	[33,34]
AlAs	12.5	5.34	5.42	3.68	[33,34]
AlSb	8.94	4.43	4.16	3.81	[32]
GaP	14.12	5.25	7.05	6.23	[32]
GaAs	11.88	5.37	5.94	5.37	[32]
GaSb	8.84	4.03	4.32	3.83	[32]
InP	10.22	5.76	4.60	4.74	[32]
InAs	8.33	4.53	3.96	4.12	[32]
InSb	6.70	3.65	3.02	2.99	[32]
ZnS	10.22	6.48	4.62	5.40	[35]
ZnSe	8.59	5.06	4.06	4.59	[36,37]
ZnTe	7.13	4.08	3.12	3.17	[35]
CdTe	5.38	3.74	2.02	2.40	[37,38]

$$\epsilon_f = \epsilon_\perp c_{11}/(c_{11}+2c_{12}) \quad \text{for } \{100\}$$
$$\epsilon_f = \epsilon_\perp (c_{11}+2c_{12}+4c_{44})/3(c_{11}+2c_{12}) \quad \text{for } \{111\} \qquad (5)$$
$$\epsilon_f = \epsilon_\perp (c_{11}+c_{12}+2c_{44})/2(c_{11}+2c_{12}) \quad \text{for } \{110\}$$

Table 3 gives the elastic constants of some semiconductor crystals and the quantity $C = 2c_{44}+c_{12}-c_{11}$, which is zero for isotropic solids. Note that the sample was assumed to be perfectly flat in Eqs. (4) and (5). If the sample is curved owing to the elastic strain, then the formulas such as Eqs. (4) and (5) of Ref. [6] must be used.

The Bragg peak position of a very thin, lattice-matched heteroepitaxial layer can be shifted because of an interference effect. This peak shifting is sometimes referred to as the Fewster–Curling–Wie effect [39,40]. Fig. 13 shows rocking curves of Ga(In)As/GaAs with a varying Ga(In)As layer thickness, calculated using a dynamical diffraction theory. With an indium mole fraction of 2.2×10^{-3} in the isoelectronic-doped Ga(In)As layer [7], the layer Bragg peak clearly shifts toward the substrate Bragg peak as the layer thickness becomes small (at 0.54 μm in Fig. 13). This effect has an important implication in the use of the peak separation $\Delta\theta$ to find the layer strain and composition. This is especially important for such lattice-matched heterostructures and superlattices as AlGaAs/GaAs and $Ga_{1-x}In_xAs/InP$ with x near 0.5 [41].

This peak-shifting effect was found to be almost independent of the sample crystal, X-ray wavelength, and the lattice plane (*hkl*), and it depended only on a product of the layer thickness and the lattice mismatch, as shown in Fig. 14 [40]. Therefore, for a thin

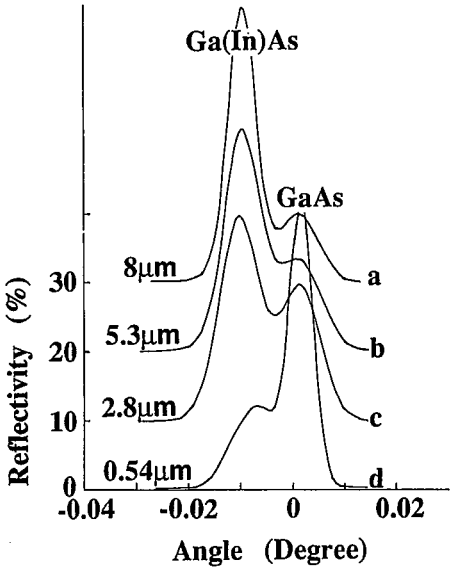

Fig. 13. Simulated 004 Cu $K\alpha_1$ Bragg profile of isoelectronic-doped Ga(In)As/GaAs as a function of the Ga(In)As layer thickness [40].

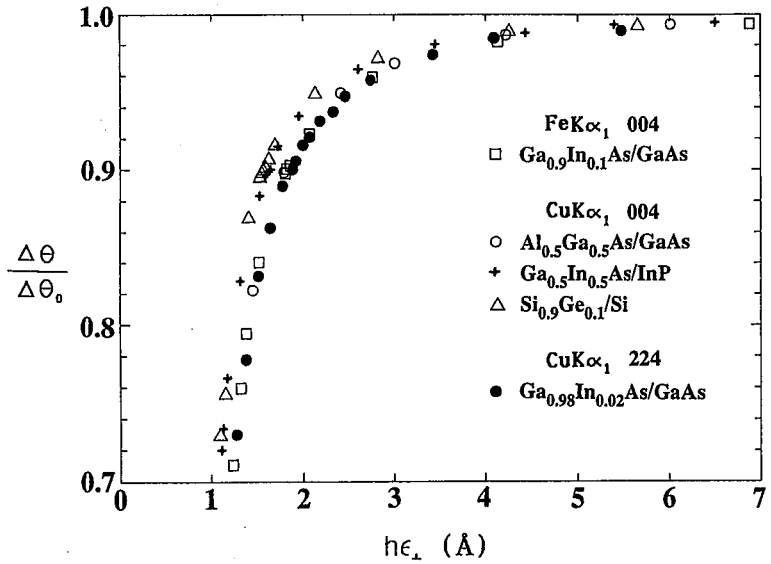

Fig. 14. Ratio of actual peak separation $\Delta\theta$ to the peak separation in the thick-layer limit $\Delta\theta_0$ as a function of the thickness–mismatch product, $h\epsilon_\perp$ [40]. Note that the peak-shifting effect is almost independent of the X-ray wavelength, sample materials and the (*hkl*) plane.

lattice-matched layer, only the dynamical theory simulation may be used, and the simple peak separation ($\Delta\theta$) method is not valid in such a case. From Fig. 14, a 3% peak shift is seen to occur at

$$h = 3(1-\nu)\epsilon_f/(1+\nu) \text{ Å} \tag{6}$$

3.2. *Rocking-curve width (FWHM)*

For a bulk crystal, the angular range of total reflection, D, is given by [42]

$$D = \frac{2\lambda^2 r_e |F_h|}{\pi\sqrt{|b|}V_c \sin(2\theta_B)} \text{ radians} \tag{7}$$

where F_h is the structure factor and other parameters are as defined in Eq. (13) and equations following. In a GaAs(001) crystal, for example, D equals 8.17 arcsec for 004 Cu Kα_1 reflection, 2.27 arcsec for 224 reflection with a large-angle incidence, and 19.2 arcsec for 224 with a small-angle incidence. For the Cu Kα_1 004 reflection, Fig. 15 shows a theoretical FWHM for a GaInAs layer (a perfect crystal), obtained from a calculated rocking curve after convolution with a Si(100) four-reflection MC profile [43]. Type and number of monochromator crystals had only a small influence on the FWHM. For a small layer thickness, Fig. 15 indicates that the theoretical FWHM for a GaInAs layer is given approximately by

$$\text{FWHM} = 18h^{-0.97} \tag{8}$$

where FWHM is in arcsec and h is in micrometers. For a layer thicker than three times the extinction depth ($3L_e \sin\theta_B$), the FWHM remains constant at a bulk FWHM, as shown in Fig. 15. For a perfect bulk crystal the theoretical FWHM depends on the X-ray wavelength: FWHM(Mo Kα) $\approx$ 0.40FWHM(Cu Kα) and FWHM(Fe Kα) $\approx$ 1.43FWHM(Cu Kα). For other wavelengths, the FWHM is proportional to $\lambda/(4d^2-\lambda^2)^{1/2}$ where d is the lattice plane spacing [42].

The experimental data on a ternary GaInAs alloy layer was recently reviewed by the present author [43]. A FWHM value much larger than the theoretical value should then be attributed to a poor layer quality due to crystal defects and strain relaxation, and to the wafer bending caused by residual stress. If each term causes a gaussian broadening in the rocking curve, then the resultant total FWHM equals

$$\sqrt{\beta_i^2+\beta_r^2+\beta_d^2} \tag{9}$$

where β_i is the intrinsic FHWM of a perfect crystal including the MC convolution, β_r is due to sample curvature, and β_d is due to defects which may arise from the poor crystal

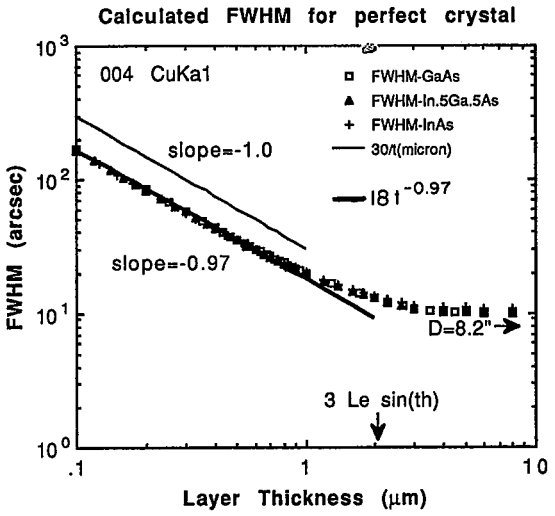

Fig. 15. Theoretical rocking-curve FWHM as a function of a perfect crystal layer thickness. For thickness smaller than about three times the extinction depth, the FWHM is almost inversely proportional to the layer thickness. Data from Ref. [43].

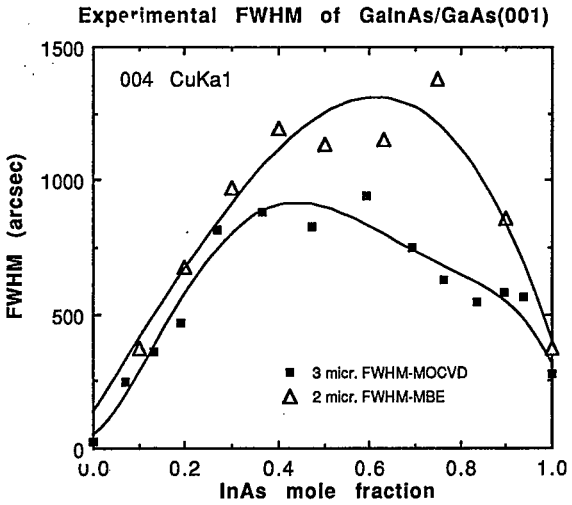

Fig. 16. Experimental 004 Cu Kα FWHM in strain-relaxed GaInAs/GaAs structure grown by MBE (△, 2-μm-thick GaInAs) and MOCVD (■, 3-μm-thick GaInAs). Data from refs. [45,46].

growth and/or from strain relaxation. For 004 Cu Kα_1, β_i can range from 200 arcsec down to 10 arcsec depending on the layer thickness, β_r from about 10 arcsec to over 100 arcsec depending on the residual stress, and β_d up to well over 1000 arcsec. Experimental FWHM data in a GaInAsP quaternary layer were discussed by Lee et al. [44].

Fig. 16 shows experimental FWHM measured on a partially strain-relaxed GaInAs layer on a GaAs(001) substrate, reported in refs. [45,46]. These data are mostly due to β_d. Contributions from β_r and β_i are negligibly small compared to β_d. The sample 2 μm thick (△) had a higher FWHM than the sample 3 μm thick (■), which can be partially attributed to the fact that over 85% of the Bragg intensity comes from the first two extinction depths (about 1.4 μm) and the crystal quality is better in regions farther away from the mismatched interface. Interestingly, for an indium composition greater than about 0.5, the FWHM decreases with the increasing mismatch, the origin of which is not clearly understood. The solid curves are polynomial fits to the data points.

3.3. Structure factor

The zinc blende and diamond structures consist of two fcc sublattices (say, α and β).

$$F_{hkl}=\begin{cases}4\,(f_\alpha+f_\beta) & \text{for } h+k+l=4n \text{ and all even}\\ 4\,(f_\alpha-f_\beta) & \text{for } h+k+l=4n+2 \text{ and all even}\\ 4\,(f_\alpha\mp if_\beta) & \text{for } h+k+l=4n\pm1 \text{ and all odd}\\ 0 & \text{otherwise}\end{cases} \tag{10}$$

where n is an integer, f_α and f_β are the atomic scattering factors [24] for atoms on each fcc sublattice, and i is the imaginary unit. For ternary and quaternary alloys, the atomic scattering factors of the constituent atoms on each sublattice must be averaged before using them in Eq. (10). The diffraction intensity is proportional to $|F_{hkl}|^2$, and the 002 and 006 reflections will have a reasonable intensity only if the difference in the average atomic number of the two sublattices is large (such as in InP, AlAs, ZnS, and GaSb). The 002 and 006 intensities will be very weak in AlP, GaAs, InSb, ZnSe and CdTe, and forbidden in Si and Ge. This very small structure factor of the 002 diffraction was used in identifying

the (defective zinc blende) Ga_2Se_3 compound in the ZnSe/GaAs interface by high-resolution transmission electron microscopy (HRTEM) [47]. In a dark-field HRTEM image, no bright or dark lines can be observed in the ZnSe and GaAs materials because of the very close values in the atomic scattering factors for Zn, Ga, As and Se. However, in the zinc blende Ga_2Se_3, where one-third of the Ga sublattice is empty, a significant 002 structure factor is expected and is responsible for the bright contrast at the interface [47].

The atomic scattering factor is a monotonically decreasing function of $\sin\theta_B/\lambda$ or equivalently of $\sqrt{h^2+k^2+l^2}$. Because of the large difference in atomic mass between In and P, a 002 reflection will produce a strong enough Bragg peak for InP(001), and therefore 002 may be used instead of 004 for samples on an InP(001) substrate. However, a 004 reflection is much preferred to 002 for samples on a GaAs(001) substrate because of the relative ease of identification of the substrate peak. The asymmetric reflections 224, 113, and 115 are all possible. In the 002 reflection, any interfacial monolayers must be carefully considered in the structure factor calculation because the two sublattices are 180° out of phase from each other.

3.4. X-Ray penetration depth

The knowledge of the X-ray penetration depth is important in interpreting the rocking-curve profile and FWHM, particularly for such depth-dependent structures as ion-implanted and thermally diffused crystals and the strain-relaxed epitaxial structures. The X-ray penetration lengths are given by

$$\begin{aligned} L &= V_c/(2\lambda r_e F_0'') = \text{normal absorption length} \\ L_e &= V_c/(2\lambda r_e F_h') = \text{extinction length} \end{aligned} \tag{11}$$

where F_0'' is the imaginary part of the structure factor of the incident beam, F_h' is the real part of the structure factor of the reflected beam and V_c is the unit cell volume. Other parameters are defined following Eq. (13).

Fig. 17 shows an X-ray penetration length for 004 Cu $K\alpha_1$ reflection in a GaAs(001) crystal as a function of the deviation from the Bragg angle, calculated based on the Darwin–Prins theory [42]. Within the Bragg profile the penetration length equals the extinction length, and outside the Bragg profile it is given by the normal absorption length. The penetration depth, $L \sin\theta_B$ and $L_e \sin\theta_B$, equals 15.9 μm and 0.74 μm, respectively,

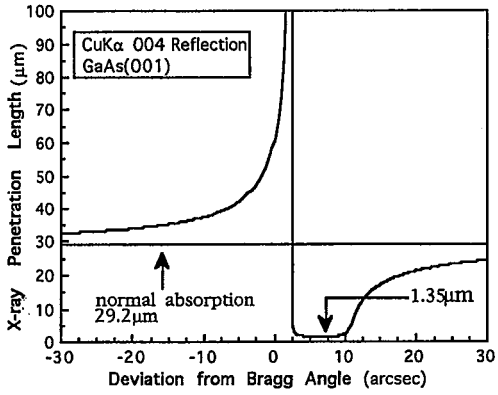

Fig. 17. X-Ray penetration length of Cu Kα radiation in GaAs as a function of the deviation from the 004 Bragg angle, calculated using the Darwin–Prins theory. For the penetration depth, multiply with $\sin\theta_B$.

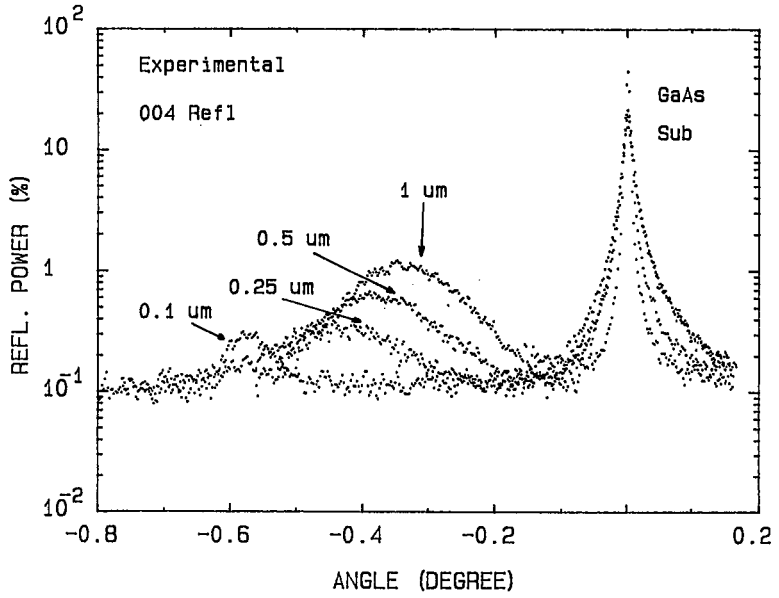

Fig. 18. Experimental 004 Fe $K\alpha_1$ rocking curves of $Ga_{0.92}In_{0.08}As/GaAs(001)$ with a different GaInAs thickness. The smaller peak separation for a thicker sample indicates an increased strain relaxation. These samples were prepared to achieve an in-plane mismatch predicted by the Dodson–Tsao model as shown in Fig. 19, in order to study the effects on deep-level traps and on the carrier transport across the dislocated heterointerface as reported in refs. [48–51].

for 004 Cu $K\alpha_1$ reflection in GaAs(001). The quality of the crystal within about $3L_e \sin\theta_B$ from the surface completely determines the rocking-curve FWHM.

3.5. Strain relaxation and critical thickness

Fig. 18 shows the 004 Fe $K\alpha_1$ rocking curves of $Ga_{0.92}In_{0.08}As/GaAs(001)$ samples with a different GaInAs layer thickness. The smaller 004 peak separation for thicker films means a smaller perpendicular mismatch and thus an increasing strain relaxation. The in-plane lattice mismatch $\epsilon_{\parallel}$ equals the amount of strain relief. A rocking curve is capable of measuring $\epsilon_{\parallel}$ greater than about 2×10^{-4}. Therefore, the critical thickness for strain relaxation, as measured by DCD, is the thickness at which the strain is relaxed by more than 2×10^{-4}. In this case, this critical thickness is much larger than the true critical thickness, which is about 200 Å thick, given by the force-balance model of Matthews and Blakeslee [52]. Typically, the X-ray critical thickness is less than that given by the energy-balance model of People and Bean [53] and larger than that given by the model of Matthews and Blakeslee, as was shown in Ref. [54] for a strained GaInAs/GaAs system. The strain relaxation can be fairly well explained by a plastic-flow model of Dodson and Tsao [55]. Fig. 19 shows a fit using the Dodson–Tsao model to the strain relaxation data by X-ray rocking curves in $Ga_{1-x}In_xAs/GaAs$ samples [54].

4. Simulation of X-ray rocking curves

The X-ray diffraction theory for describing the reflection of X-rays at the surface of an infinitely thick non-absorbing crystal was developed in the 1910s by Darwin [56] and Ewald [57]. This dynamical diffraction theory was modified by Prins in 1930 [58] by introducing

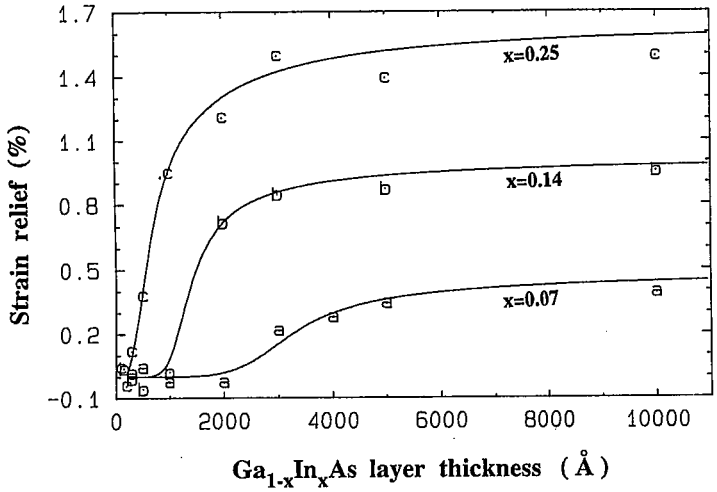

Fig. 19. Strain relief (in-plane mismatch) as a function of the GaInAs layer thickness, experimental data (letter symbols) and a theoretical fit (solid line) based on the Dodson–Tsao model. Data from Ref. [54].

a complex attribute to the theory to account for the absorption, and this successfully explained the characteristic asymmetric diffraction profile of an absorbing crystal. The X-ray diffraction theory for distorted crystals with non-uniform strain fields was developed in the 1960s by Takagi [59,60] and Taupin [61] in order to describe diffraction by curved crystals and to calculate the contrast of dislocations in X-ray topographs. In the 1970s, structural characterization of epitaxial, ion-implanted and thermally-diffused crystals became important in the fabrication of solid-state devices such as laser diodes and integrated circuits. X-Ray diffraction in the reflection mode (Bragg case) was employed for such purposes [62,63]. Also, physical understanding of the various characteristics of the diffraction profiles attracted much attention in the interest of developing a simple and practical analysis theory.

Semikinematical models, which combined thin layers in a kinematical approximation and a substrate in the full dynamical theory, were developed in order to analyze the diffraction profiles from ion-implanted crystals [8,64,65] and superlattices [66]. Kinematical models for superlattices had been developed earlier [67–69]. These semikinematical and kinematical models are not appropriate for the reflectivity greater than 10%. Also, the semikinematical models which combine the kinematical layer intensity with the dynamical substrate intensity [64] cannot be used if the layer is very thin and nearly lattice-matched because of the peak-shifting or Fewster–Curling–Wie effect (see Section 3.1). Klar and Rustichelli [70] simplified the Takagi–Taupin equation of dynamical diffraction for application to the case where the sample is laterally uniform and the strain varies only in depth. Larson and Barhorst [71] numerically integrated this simplified differential equation and simulated the rocking-curve profile for a boron-diffused silicon crystal.

An analytic solution of this simplified equation was obtained [72,73], and for computer simulation of rocking curves the solution was recursively applied to each layer in a heteroepitaxial sample. The relation of this analytic solution with the Darwin–Prins formula of an infinitely thick crystal [42] was clarified by Wie et al. [74] and Bartels et al. [75]. For the simulation of the SL rocking curves, however, the dynamical theory recursive formulas render redundancy in the calculation because an identical calculation repeats for each period. A matrix approach, which greatly facilitates the dynamical theory superlattice calculation, has been developed by Wie [41]. Other types of dynamical diffraction theories

which are not directly based on the Takagi–Taupin formalism or are more directly related to the Maxwell equations are also available [6,76–78] but do not seem to be greatly used. I shall briefly overview the dynamical and kinematical X-ray diffraction theories. The dynamical theories presented here are based on the Takagi–Taupin equation.

4.1. Takagi–Taupin theory of dynamical diffraction

General summary of the theory

The Takagi–Taupin theory of dynamical diffraction is a first-order approximation to the Maxwell (or Schroedinger) wave equation for an X-ray (or electron) wave propagating in a distorted crystal medium. The displacement **u** of lattice atoms due to deformation is assumed to be macroscopic, i.e. its variation over one X-ray wavelength (about 1 Å) is small, i.e. $\lambda du/dx \ll 1$. Also, the displacement field **D** and the polarization **P** and their first derivatives are of macroscopic variation. The dielectric susceptibility in the X-ray frequency domain is small being of the order 10^{-6}, and therefore **P** is small being of the order 10^{-6}**D**. By expanding the wave fields in a Fourier series and neglecting the second and higher order terms in **P**, d**D**/dx, and d**u**/dx, one obtains the so-called Takagi–Taupin (T–T) equation, a coupled linear partial differential equation for the incident (D_0) and diffracted (D_h) amplitudes. The T–T equation describes an interchange of energy between the two amplitudes as they propagate in the crystal medium, and therefore it is a dynamical theory:

$$\begin{aligned} \mathrm{i}\frac{\lambda}{\pi}\frac{\partial D_0}{\partial s_0} &= p\chi_{-h}D_h \\ \mathrm{i}\frac{\lambda}{\pi}\frac{\partial D_h}{\partial s_h} &= p\chi_h D_0 - 2\beta_h D_h \end{aligned} \tag{12}$$

where λ is the X-ray wavelength, s_0 and s_h are the oblique coordinates parallel to the incident and reflected wave vectors, respectively, χ equals 4π times the dielectric permitivity, and the subscript h represents the hth Fourier component corresponding to the diffracting lattice plane (hkl) or equivalently to the reciprocal lattice vector **h**. The differential operator has the meaning that $\partial/\partial s_0 = \hat{\mathbf{k}}_0 \cdot \nabla$, etc., where $\hat{\mathbf{k}}_0$ is the unit vector parallel to $\mathbf{k}_0$[1]. Other parameters are defined as follows:

$$\begin{aligned} p &= \begin{cases} 1 & \text{for normal polarization} \\ \cos 2\theta_B & \text{for parallel polarization} \end{cases} \\ \chi_h &= -\frac{r_e\lambda^2}{\pi}\frac{F_h}{V_c} \\ \beta_h &= \frac{2\mathbf{k}_0\cdot\mathbf{h}' + h'^2}{2K^2} \\ \mathbf{h}' &= \mathbf{h} - \nabla[\mathbf{h}\cdot\mathbf{u}] \\ \mathbf{k}_0 &= \mathbf{K}_0 + \frac{1/2\chi_0 K}{\gamma_0}\mathbf{n} \\ \gamma_0 &= \mathbf{k}_0\cdot\mathbf{n}/k_0 \end{aligned} \tag{13}$$

[1]The **k** (lower case) refers to wave vector inside the crystal medium and **K** (upper case) to outside the crystal medium.

where θ_B is the Bragg angle of the undisturbed crystal lattice, r_e ($=2.81794\times10^{-5}$ Å) is the classical electron radius, V_c is the unit cell volume, F_h ($=F_h'+iF_h''$) is the structure factor of the undisturbed crystal, **is the unit vector parallel to the** *inward* surface normal, and K ($=1/\lambda$) is the wave number in vacuum. Here p is the polarization factor, β_h is the strain and angular parameter, $\mathbf{h}'$ is the 'local' reciprocal lattice vector of the distorted crystal [60], and γ_0 is the direction cosine of the incident wavevector.

Heteroepitaxial samples

In a uniformly strained heteroepitaxial layer where the lattice mismatch relative to the substrate is $\epsilon_\parallel$ and $\epsilon_\perp$, parallel and perpendicular to the surface respectively, it can be shown that

$$\begin{aligned}&\mathbf{h}'=h(\epsilon_\parallel-1)\sin\phi\mathbf{i}+h(\epsilon_\perp-1)\cos\phi\mathbf{n}\\&\beta_h=2e_\parallel\cos(\theta-\phi)+e_\perp[2\sin(\theta-\phi)+\chi_0/\sin(\theta-\phi)]+2(e_\parallel{}^2+e_\perp{}^2)\end{aligned}\tag{14}$$

where

$$e_\parallel=(\epsilon_\parallel-1)\sin\theta_B\sin\phi;\quad e_\perp=(\epsilon_\perp-1)\sin\theta_B\cos\phi$$

$$\epsilon_\parallel=(d_\parallel-d_s)/d_s;\quad\text{and }\epsilon_\perp=(d_\perp-d_s)/d_s$$

Here ϕ is the angle between the sample surface and the lattice plane (*hkl*), $\theta-\phi$ is the grazing angle of incidence, $\mathbf{i}$ is the unit vector along the x axis (parallel to surface) as defined in Fig. 8. Note that the reference lattice is the substrate crystal lattice and thus θ_B is the substrate Bragg angle. The above expression for β_h is appropriate for superlattice and MQW rocking curves, where a rather wide angular scan is required. For heteroepitaxial samples where the total range of angular scan is small, the following approximate expression can be used for β_h:

$$\beta_h\approx-\sin 2\theta_B[(\theta-\theta_B)+k_\perp\epsilon_\perp+k_\parallel\epsilon_\parallel]+\frac{1-b}{b}\chi0\tag{15}$$

where

$$k_\perp=\cos^2\phi\tan\theta_B+\sin\phi\cos\phi;\quad k_\parallel=\sin^2\phi\tan\theta_B-\sin\phi\cos\phi;$$

$$b=\gamma_0/\gamma_h;\ \gamma_0=\sin(\theta_B-\phi);\quad\text{and }\gamma_h=-\sin(\theta_B+\phi)$$

Here, γ_h is the direction cosine of the diffracted wavevector relative to the inward surface normal.

4.2. Dynamical theory simulation of X-ray rocking curves

For epitaxial structures, ion-implanted semiconductors and thermally diffused samples where the strain and composition are uniform laterally and non-uniform in depth, the Takagi–Taupin equation can be further simplified using $\partial/\partial s_0=-\gamma_0\,\mathrm{d}/\mathrm{d}z$ and $\partial/\partial s_h=-\gamma_h\,\mathrm{d}/\mathrm{d}z$, where z is the coordinate axis parallel to the outward surface normal (see Fig. 8). Then, the two coupled first-order partial differential equations yield a single equation:

$$\mathrm{i}\frac{\sqrt{\gamma_0|\gamma_h|}}{\sigma}\frac{\mathrm{d}X}{\mathrm{d}z}=DX^2+2CX+B\tag{16}$$

where

$$X = \frac{D_h}{D_0\sqrt{|b|}} = \text{scattering amplitude},$$

$$B = -\frac{pF_h}{F_h'}; \quad C = -\frac{\pi\sqrt{|b|}}{\lambda\sigma}\beta_h; \quad D = -\frac{pF_{-h}}{F_h'}; \quad \sigma = \frac{r_e\lambda}{V_c}F_h'$$

Here, $(2\sigma)^{-1}$ is the extinction length for normal polarization (see Eq. (11)), and the structure factor F_{-h} corresponds to the reciprocal lattice vector $-\mathbf{h}$ or equivalently to the reflecting lattice plane $(\bar{h}\bar{k}\bar{l})$. Note that this equation is not applicable to simulating the TCD diffuse-scattering profile, because this equation is valid only for laterally uniform samples and the diffuse scattering in TCD is caused also by lateral non-uniformity. The diffuse-scattering profiles and isointensity contours may be simulated using Eq. (12), as will be described later. It is also worth noting that in most experimental conditions of HRXRD where multiple reflections are involved (a minimum of two reflections in DCD and three in TCD), the parallel-polarization portion is negligibly small in the measured X-ray because $\cos 2\theta_B$ is usually small, and p may be taken to be unity (normal polarization dominant). For a uniform crystal plate, Eq. (16) can be solved analytically and this solution forms the basis for rocking-curve simulation in a lamellar approximation [72,74,75].

Recursive formula approach

Referring to Fig. 20 showing a layer structure, an analytic solution at the surface of the jth layer of thickness t_j, may be given as

$$X_j = \frac{S_jX_{j-1} - i(B_j + C_jX_{j-1})\tan(S_jA_j)}{S_j + i(C_j + B_jX_{j-1})\tan(S_jA_j)} \tag{17}$$

where

$$X_j = X(z_j); \quad S_j = \sqrt{C_j^2 - B_jD_j}; \quad A_j = \sigma t_j/\sqrt{\gamma_0|\gamma_h|}$$

Therefore if the scattering amplitude X_{j-1} at the surface of layer $j-1$ is known then the scattering amplitude at the surface of jth layer can be calculated. Eq. (17) is applied recursively to each layer, starting from the surface of the substrate ($j=0$), and ending at the surface of the top layer ($j=n$). The substrate solution therefore serves as a boundary condition and can be obtained by setting the layer thickness t_0 equal to infinity in Eq. (17) [74].

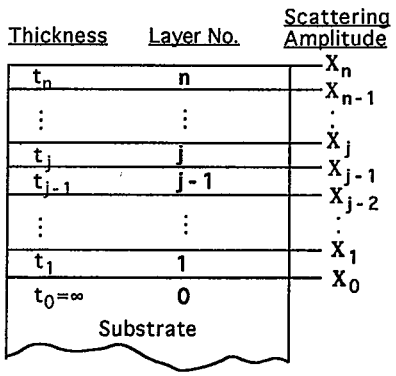

Fig. 20. Layer schematics for rocking-curve simulation.

$$X_0 = -\frac{B_0}{C_0 - S_0} \tag{18}$$

The recursive-formula approach can be used for any heterostructure sample and in a lamellar approximation for a continuously varying strain such as in ion-implanted and thermally diffused crystals.

Matrix approach

For SL and MQW samples, the calculation is identical for each period. In a matrix form, the repetition of the same calculation for different periods can be avoided, whereas this is not possible in the case of the recursive formula (Eq. (17)). This matrix method [41] is particularly useful in analyzing SL rocking curves to obtain information on the interface structures. A period of a SL can consist of several layers if the interfacial transition layers (or atomic planes) are included.

The recursive formula Eq. (17) can be put into the following form:

$$X_j = \frac{P_j X_{j-1} + Q_j}{V_j X_{j-1} + W_j} \tag{19}$$

where the layer parameters are

$$P_j = S_j - \mathrm{i}C_j \tan(S_j A_j); \quad Q_j = -\mathrm{i}B_j \tan(S_j A_j);$$

$$V_j = \mathrm{i}D_j \tan(S_j A_j); \quad W_j = S_j + \mathrm{i}C_j \tan(S_j A_j)$$

The rocking curve for the sample shown in Fig. 20 can be obtained from

$$X_n = \frac{P_s X_0 + Q_s}{V_s X_0 + W_s} \tag{20}$$

where

$$\begin{pmatrix} P_s & Q_s \\ V_s & W_s \end{pmatrix} = \begin{pmatrix} P_n & Q_n \\ V_n & W_n \end{pmatrix} \cdots\cdots \begin{pmatrix} P_2 & Q_2 \\ V_2 & W_2 \end{pmatrix} \begin{pmatrix} P_1 & Q_1 \\ V_1 & W_1 \end{pmatrix}$$

For a SL and MQW with N periods and m layers per period, the dynamical-theory rocking curve can be obtained from Eq. (20), but with

$$\begin{pmatrix} P_s & Q_s \\ V_s & W_s \end{pmatrix} = \begin{pmatrix} P_p & Q_p \\ V_p & W_p \end{pmatrix}^N \qquad \text{for a SL with } N \text{ periods} \tag{21}$$

where the period matrix is

$$\begin{pmatrix} P_p & Q_p \\ V_p & W_p \end{pmatrix} = \begin{pmatrix} P_m & Q_m \\ V_m & W_m \end{pmatrix} \cdots\cdots \begin{pmatrix} P_2 & Q_2 \\ V_2 & W_2 \end{pmatrix} \begin{pmatrix} P_1 & Q_1 \\ V_1 & W_1 \end{pmatrix} \tag{22}$$

Here, the Nth power of the period matrix is taken after diagonalizing the period matrix. Calculation using this approach greatly facilitates the computation if the number of layers per period is more than two, as should be the case when the interface structures are considered.

4.3. Semi-kinematical theory simulation

For a thin multilayer structure, the layer diffraction amplitudes may be approximated by a kinematical formula with the substrate amplitude still given by the dynamical formula.

A semikinematical theory approximates the dynamical theory well if the layer reflectivity is less than about 10% [75,41]. In a very thin layer the layer peak can be shifted in angular position because of an interference effect between the diffraction amplitudes of the layer and the substrate [39,40]: the layer diffraction amplitude must have a phase consistent with the substrate amplitude [41]. Such a semikinematical theory is presented below.

The diffraction amplitude due to n layers (see Fig. 20) is the sum of the amplitudes due to each layer, multiplied by an adequate phase and absorption factor.

$$X_{\text{layer}} = \mathrm{i}\sum_{j=1}^{n} a_j \exp[-\mathrm{i}(A_j Y_j + \Phi_j)] \frac{\sin(A_j Y_j)}{Y_j} \tag{23}$$

where Y is the real part of C

$$a_j = \exp\left[-\frac{\gamma_0 + |\gamma_h|}{2\gamma_0|\gamma_h|} \sum_{i=j+1}^{n} \mu_i t_i\right] = \text{absorption factor}$$

$$\mu_j = \lambda r_e (F_0'' + F_h'')/V_c = \text{absorption coefficient of the } j\text{th layer, and} \tag{24}$$

$$\Phi_j = 2\sum_{i=j+1}^{n} A_i Y_i = \text{phase delay due to the layers lying above the } j\text{th layer}$$

The semikinematical diffraction amplitude of the sample is then

$$X_n = X_{\text{layer}} + a_0 \exp(-\mathrm{i}\Phi_0) X_0 \tag{25}$$

This model was shown to agree rather well with the dynamical theory for samples with thin epitaxial layers [41] (this semikinematical theory is called amplitude-boundary-condition (ABC) formula in Ref. [41]). A similar semikinematical theory developed by Speriosu [64] combines the kinematical reflectivity of layers, $|X_{\text{layer}}|^2$, with a dynamical reflectivity, $|X_0|^2$, and thus it does not account for a possible interference effect between the two amplitudes [41].

Figs. 21 and 22 show the experimental and simulated X-ray rocking curves for a single-layer structure and a superlattice structure, respectively, originally reported in Ref. [41]. The three simulated curves are using the above semi-kinematical theory (ABC-kinematical), the dynamical theory in the matrix approach (Section 4.2), and the semikinematical model combining the intensities (IBC-kinematical) rather than amplitudes. The samples presented in Fig. 21 are 0.88 μm $Al_{0.37}Ga_{0.63}As$/GaAs(001) and 0.65 μm $In_{0.535}Ga_{0.465}As$/InP(001) single-layer structures, measured after a successive chemical etching. The superlattice sample in Fig. 22 is a 50-period 146-Å $Al_{0.8}Ga_{0.2}As$/146 Å GaAs on a GaAs(001) substrate, also measured after a successive chemical etching. Both figures show that the above semikinematical theory properly accounts for the peak-shifting effect for thin layers. Had the aluminum content been smaller than 0.8 (or smaller average mismatch) in the AlGaAs layer of the superlattice sample in Fig. 22, the peak-shifting effect of the zero-order peak in the smaller total-SL-thickness samples would have been more dramatic than that shown by Fig. 22. For the SL samples, the zero-order peak manifests the peak-shifting effect, while all higher-order peaks may not show such an effect [40].

4.4. Comparison of kinematical X-ray diffraction and optical Fraunhofer diffraction

Double-crystal X-ray diffraction of a heterostructure is similar to the optical Fraunhofer diffraction of a line grating. I will illustrate this for three different cases: a single heteroepitaxial

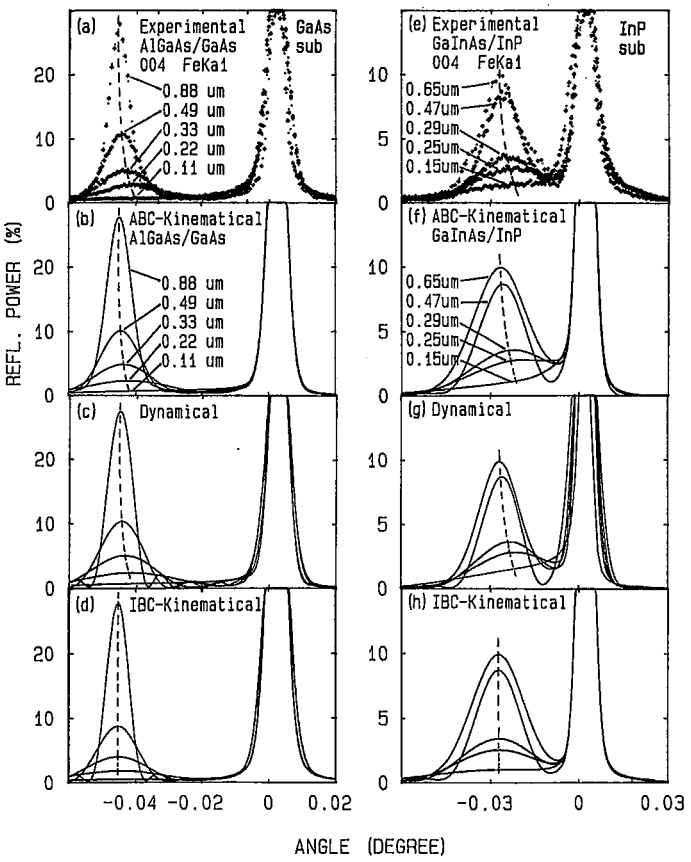

Fig. 21. Experimental and simulated X-ray rocking curves for 0.88-μm $Al_{0.37}Ga_{0.63}As$/GaAs(001) and 0.65-μm $In_{0.535}Ga_{0.465}As$/InP(001) single-layer structures, as a function of the epi-layer thickness. Data obtained after a successive chemical etching [41].

layer, a quantum-well structure, and a superlattice (or MQW) structure. The normal absorption in the X-ray diffraction will be neglected.

For a *single layer*, a normalized layer diffraction intensity may be given as

$$I_{\text{layer}} = \frac{\sin^2\phi}{\phi^2} \tag{26}$$

where

$$\phi = AY = \frac{\pi \sin 2\theta_B}{|\gamma_h|\lambda} t(\Delta\theta + k_\perp \epsilon_\perp)$$

$\epsilon_\perp$ is the perpendicular mismatch of the layer relative to the substrate, and $\Delta\theta$ is the deviation of the incident angle from the substrate Bragg angle. Here, ϕ is the phase change in the X-ray wave field as the wave traverses half the layer thickness t. (Note that this ϕ is not same as the angle parameter ϕ used in the previous section.)

Fig. 23 illustrates the similarity between an X-ray rocking curve of a single-layer heteroepitaxial sample and the optical Fraunhofer diffraction by a single line slit. The layer fringe peaks (the so called *Pendellösung fringes* or equivalently *thickness fringes*) appear whenever $\phi = n\pi$ with n a non-zero integer. The layer thickness t can be found from the spacing of the Pendellösung fringe peaks $\delta\theta$ by

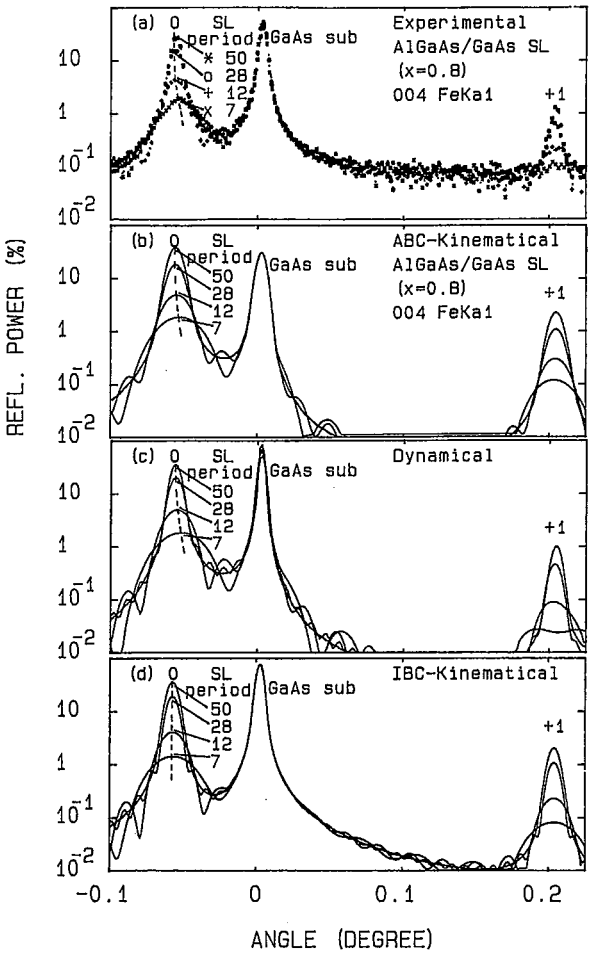

Fig. 22. Experimental and simulated rocking curves of a 50-period SL with 146 Å $Al_{0.8}Ga_{0.2}As$/146 Å GaAs on a GaAs(001) substrate. The semikinematical theory, eqs. (23) and (25), also gives the peak-shifting effect. Data from Ref. [41].

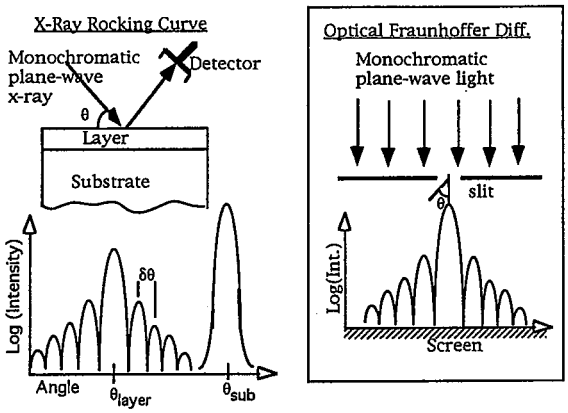

Fig. 23. X-Ray rocking curve by a single-layer heteroepitaxial sample vs. optical Fraunhofer diffraction by a single slit.

$$t = \frac{|\gamma_h|\lambda}{\delta\theta \sin 2\theta_B} \tag{27}$$

If the angle resolution is 10 arcsec for the fringe peaks, then the maximum layer thickness that can be determined from the Pendellösung fringe spacing is about 2.25 μm, with $\lambda = 1.54$ Å and $\theta_B = 45°$. This maximum thickness that can be measured from the Pendellösung fringes is in a reasonable agreement with an experiment where the Pendellösung fringes could be observed for an AlGaAs layer 0.5–2.0 μm thick [79]. The envelope function to the Pendellösung fringe peaks ($\sin^2\phi$ is unity) is ϕ^{-2}. Note that ϕ^{-2} is the intensity profile of the crystal truncation rod for the smooth and abrupt surface and interface (see Sections 2.1 and 5.1.1). Since the envelope to the thickness fringe peaks is the CTR profile, the degree of damping of higher-order fringe peaks can be a measure of the interface roughness (see Section 5.1.1).

For a *quantum well* structure, Fig. 24 shows a schematic illustration of the X-ray diffraction near the layer-B Bragg angle and the optical Fraunhofer diffraction by two open line slits. A kinematical expression for the rocking curve profile near the layer-B Bragg peak is [11]

$$I_{QW} = \frac{\sin^2\phi_b}{\phi_b^2} \cos^2(\phi_a + \phi_b) \tag{28}$$

Here, the cosine term represents interference between the wave fields diffracted by the two B layers, and near the Bragg peak (at $\phi_b = 0$) its *phase is proportional to* $t_a \Delta\epsilon_\perp$ where $\Delta\epsilon_\perp = \epsilon_{a,\perp} - \epsilon_{b,\perp}$. Generally,

$$\phi \propto t\epsilon \tag{29}$$

This interference effect not only can introduce an interference structure within the layer-B Bragg peak profile, but also can modulate the Pendellösung fringe peaks given by the sine term. The interference effect is used for characterization of interfaces and strained quantum wells with a submonolayer resolution.

For *superlattice* and *multiple quantum well* structures with N periods and a period composed of two layers (a and b), a kinematical expression for the total SL reflectivity is

$$I_{SL} = |X_p|^2 H \tag{30}$$

where,

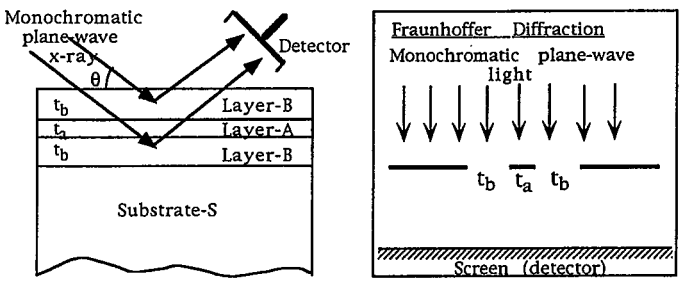

Fig. 24. X-Ray diffraction by the B-layer (barrier) in a B/A/B/substrate structure vs. optical Fraunhofer diffraction by two open slits.

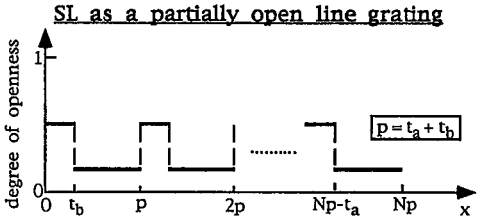

Fig. 25. Model of a SL with two layers per period as a line grating consisting of two partially transparent slits.

$$X_p = A_a \frac{\sin\phi_a}{\phi_a} \exp(-i\phi_p) + A_b \frac{\sin\phi_b}{\phi_b} = \text{period amplitude},$$
$$I^{(0)} = N^2|X_p|^2 = \text{envelope function}, \quad \text{and} \tag{31}$$
$$H = \frac{\sin^2 N\phi_p}{\sin^2\phi_p} = \text{interference function}$$

where $\phi_p = \phi_a + \phi_b$, the phase shift over half the period thickness. The Eq. (30) is identical in form to the optical Fraunhofer diffraction by a simple line grating [80] except that the period function of SL has two terms (Eq. (31)) because both layers in the period can reflect X-ray, compared with only one term in the optical line grating. Fig. 25 shows a modeling of a two-layer period SL as a line grating with two partially transparent slits per period with a different degree of 'openness'. The nth-order SL peak occurs at $\phi_p = n\pi$, where n is an integer, with its peak intensity given by $N^2|X_p|^2$ (the envelope function). The SL periodicity p is determined from the angular spacing ($\delta\theta$) of the principal SL peaks by

$$p = \frac{|\gamma_h|\lambda}{\delta\theta \sin 2\theta_B} \tag{32}$$

The principal SL peaks (ϕ_p = integer times π) are the thickness fringes corresponding to *one period*. In between the two neighboring principal peaks there are $N-2$ secondary peaks ($N\phi_p$ = integer times π plus $\pi/2$), which are the thickness fringes corresponding to the total SL thickness. If the layer thicknesses are such that $t_a:t_b = m:n$ where m and n are integers, then every $(m+n)$th SL peak intensity is close to zero, with its non-zero intensity proportional to the square of the perpendicular mismatch between the two layers. When some highly strained molecular planes are present at the interface, they affect very sensitively both the angular position of the zero order SL peak ($\Delta\theta_0$) and the envelope function profile ($N^2|X_p|^2$), and they both serve as means towards analyzing the SL interface (see Section 5.1.2).

5. Analysis of interfaces and quantum device structures

When both the cation and anion change in a heterojunction, different interfacial structures are possible, and usually the interfacial monolayers are highly strained (as much as 3.5% or 7% in strain, as discussed in Section 1.2). According to the cation constituents, a III–V heterointerface may be described as the (P,As) interface for such structures as GaInP/GaAs, GaInAs/InP and GaInAsP/InP, and as the (As,Sb) interface for InAs/GaSb and InAs/AlSb. Apparent differences in interface composition have been reported to produce substantial changes in structural and electronic properties in the (As,Sb) system [81–84]. In this section, I will discuss the diffraction principles and some published data on the

DCD analysis of interfaces, strained quantum wells and optoelectronic devices. For interface analysis, I will consider only such lattice-matched structures as GaInP/GaAs, ZnSe/GaAs, GaInAs/InP, AlGaAs/GaAs, etc. In the discussion I will consider the rocking curves simulated by the dynamical diffraction theory, interpreted using the kinematical diffraction principles. Some recently published data are also discussed.

5.1. Interface analysis with submonolayer resolution

One of the following two diffraction principles can be utilized in the interface analysis: (i) the relative phase shift is proportional to the thickness–mismatch product (see Eq. (29)); and (ii) the intensity profile of the crystal truncation rod is sensitive to the interface (and surface) sharpness. I shall refer to the former principle as the *phase rule* and the latter as the *CTR rule*. The phase rule can explain the effect of the highly strained interfacial molecular planes such as in GaInAs/InP and can be used to analyze the interface with submonolayer resolution. The highly strained interfacial monolayers can have a sensitive effect on the Bragg peak profile and on the Pendellösung-fringe peaks. The CTR rule explains the effect of interface grading on the rocking-curve profile when no such highly strained interfacial molecular planes are present, as in the case of AlGaAs/GaAs, and provides a typical thickness sensitivity of 100–200 Å.

5.1.1. Single heteroepitaxial layers

Phase rule

In Sections 1.2 and 2.2, I briefly described the high sensitivity of X-ray diffraction to the thickness of highly strained interfacial molecular planes in certain lattice-matched heteroepitaxial systems. Examples are GaInAs/InP, GaInP/GaAs, InAs/GaSb, ZnSe/GaAs, and CdTe/InSb. In an ideally abrupt GaInP/GaAs interface, for example, the interfacial (004) planes in the [001] direction may be either -Ga-As*-GaIn-P- or -As-Ga*-P-GaIn- where the highly strained molecular plane is marked by '*', with $\epsilon_\perp = +7.6\times10^{-2}$ for GaInAs and $\epsilon_\perp = -7.1\times10^{-2}$ for GaP. An extremely high thickness-sensitivity of the rocking-curve profile can be best understood from the kinematical rocking-curve profile of a B/A/B/ substrate sandwich structure (see Eq. (28)).

Fig. 26 shows calculated (dynamical theory without instrumental convolution) 004 Cu $K\alpha_1$ rocking curves of a 0.3 μm $Ga_{0.47}In_{0.53}As$/InP(001) sample for four possible interfacial structures. The matrix method of the dynamical diffraction theory was used for the calculation (see Eq. (20)). Fig. 26A and Fig. 26B are the atomically abrupt interfaces with the (004) interfacial planes given by In-P*-GaIn-As and P-In*-As-GaIn, respectively. Fig. 26C and Fig. 26D are for interfaces with one transitional, group-V atomic plane, and hence the (004) interfacial planes are In-P*-GaIn*-$As_{0.5}P_{0.5}$*-GaIn-As and P-In*-$As_{0.5}P_{0.5}$*-GaIn-As, respectively. An asterisk indicates the highly strained molecular planes. In this particular example, the left-hand shoulder of the 004 InP Bragg peak is different depending on whether the top atomic plane of the InP substrate is P (Fig. 26A) or In (Fig. 26B). The profile of GaInAs Pendellösung fringe peaks, at the negative angles in particular, is sensitive to an atomic-level interfacial grading of the group-V sublattice (Fig. 26C and Fig. 26D). A similarly sensitive rocking-curve variation is expected in the lattice-matched GaInP/GaAs, ZnSe/GaAs, and InSb/CdTe heterostructures. The epitaxial growth process could be 'fine-tuned' for an optimum interfacial structure by using the double-crystal rocking curve as a quick, non-destructive characterization tool.

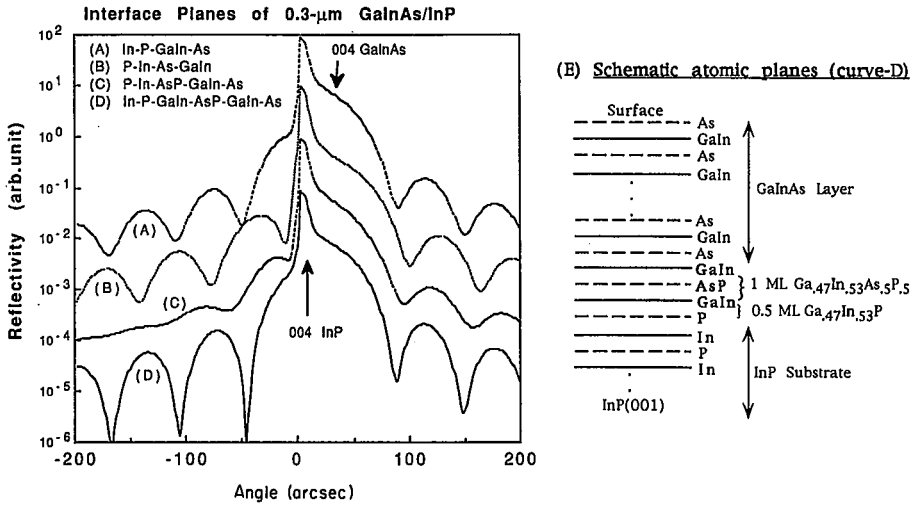

Fig. 26. Simulated 004 Cu $K\alpha_1$ rocking curves of 0.3-μm $Ga_{0.47}In_{0.53}As$/InP(001) for four possible interfacial structures. Curves (A) and (B) are with an atomically abrupt interface, and curves (C) and (D) are with an additional AsP transition plane in the group-V sublattice. (E) is the atomic layer schematic for curve (D).

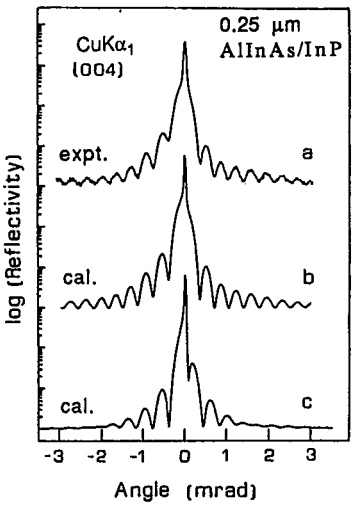

Fig. 27. Experimental and simulated rocking curves of AlInAs/InP: curve (a), experimental 004 Cu $K\alpha_1$ rocking curve; curve (b), simulation with an InAs interface layer 5 Å thick, an $Al_{0.472}In_{0.528}As$ interlayer 500 Å thick and a lattice-matched $Al_{0.475}In_{0.525}As$ epi layer 2000 Å thick; curve (c), as in curve (b) without the InAs interface layer or any interface layer. Data from Ref. [85].

Recently, Giannini et al. [85] analyzed an MBE-grown GaInAs and AlInAs layer nominally lattice-matched to InP(001). Fig. 27 shows that for AlInAs/InP, the simulated rocking curve profile (both the Bragg peak profile and the Pendellösung fringe profile, Fig. 27, curve (b)) agrees with the experimental rocking curve (Fig. 27, curve (a)) only if an interfacial InAs layer 5 Å thick is included [85]. Fig. 27 also shows that not only the detailed Bragg profile but also the higher-order fringe peaks are sensitive to the interfacial structure. With some thin strained interfacial layers included, the higher-order fringe peaks are more clearly visible, as curve (b) in Fig. 27 shows. However, curves (B) and (C) in Fig. 26 show that the higher-order fringe peaks do not always become more visible with increased numbers of interfacial planes.

For a ZnSe/GaAs interface, an interfacial Ga_2Se_3 layer about 2 ML thick was reported to exist in high-resolution TEM work. The Ga_2Se_3 was a zinc blende structure with one-third of the Ga sites left as vacancies [47]. The lattice parameter is about 5% smaller than that of GaAs or ZnSe (they used $\epsilon_\perp = -6.4\%$ in their model analysis) owing to the vacancies. This rather well-defined transition layer was formed on As-deficient GaAs surfaces. In different growths, less well-defined interfacial layers were also observed [86]. Therefore, the well-defined interfacial Ga_2Se_3 layer may be found only in certain carefully prepared samples, but this could be easily distinguished by a rocking-curve analysis. In the fitting analysis, if the defected zinc blende III_2VI_3 strained interfacial layers do not give a good fit to the data then more diffuse interfacial layers may be tried. I discuss this type of graded interface in CdTe/InSb in the next section.

CTR rule

A high sensitivity of the rocking-curve profile to the interfacial atomic structure is not expected in lattice-matched structures such as AlGaAs/GaAs, AlInAs/GaInAs, AlSb/GaSb, and AlP/GaP, because highly strained molecular planes are not present at the interface. However, the crystal truncation rod is sensitive to the surface roughness. The CTR profile near the Bragg peak, in the surface normal direction, is proportional to $[\sin \frac{1}{2} qa]^{-2}$ for an ideally smooth surface, and to $[\sin \frac{1}{2} qa]^{-4}$ for a very rough or gradual surface where a is the lattice constant [29]. For a heteroepitaxial layer of finite thickness, the CTR will occur owing to the truncation of the crystal layer both at the free surface and at the heterointerface, and this CTR profile forms an envelope function to the thickness fringe peaks, as was discussed in Section 3.4. The envelope (CTR) function to certain portions of the thickness fringe peaks may be

$$\text{envelope} \propto \begin{cases} \Delta\theta^{-2} & \text{for an ideally abrupt interface} \\ \Delta\theta^{-4} & \text{for a very rough interface} \end{cases} \tag{33}$$

where $\Delta\theta$ is the deviation from the layer Bragg angle. For samples with an intermediate interface roughness, the envelope function will be proportional to $\Delta\theta^{-s}$ with $2 < s < 4$. (The envelope function may actually appear very complicated. These simple forms are only for a discussion purpose.) The higher-order fringe peaks will therefore decay faster for a graded interface than for a sharp smooth interface, which can be a tool for interface characterization. A different degree of damping of the higher-order fringe peaks was used as a measure of the interface roughness in AlGaAs/GaAs and GaAs/AlGaAs/GaAs [87], and the sensitivity of a DCD rocking-curve profile to the interface width was about 100–200 Å in these structures, which may be compared to the 1.6-Å sensitivity in the GaInAs/InP structure (Fig. 26). It is also useful to note that the intensity of the Pendellösung fringe peaks on the higher-angle side increases strongly while decreasing on the lower-angle side, or vice versa, depending on the sign and magnitude of the strain gradient at the interface [87–89].

5.1.2. *Superlattice and MQW*

Interfaces in a superlattice can be analyzed using the following two features in the rocking curve: (i) the zero-order SL peak position and (ii) the overall SL peak profile. I shall discuss these two features using a simple kinematical model and then use them in the discussion of rocking-curve analysis of such samples as GaInP/GaAs and ZnSe/GaAs with a highly strained interfacial monolayer.

Kinematical principle

The SL periodicity (see Eq. (32)) must include the interfacial planes.

$$p = \sum t_j \tag{34}$$

Another constraint exists if the zero-order SL peak can be identified in the experimental data. Theoretically, the zero-order peak occurs at an angular position $\Delta\theta_0$ at which ϕ_p equals zero, and thus

$$\Delta\theta_0 = -\frac{k_\perp}{p} \sum t_j \epsilon_{\perp j} \tag{35}$$

The envelope function will have more terms than the Eq. (31) shows, as many more terms as the number of interfacial transition layers, and its angular profile will depend on the detailed interface structure, thus affecting the SL peak intensities. If the SL rocking curve is calculated using the matrix approach of the dynamical theory (see Section 4.2), then the envelope function can be easily calculated from the period matrix elements Q_p and W_p (see Eq. 22) by

$$I^{(0)} = N^2 |Q_p / W_p|^2 = \text{envelope function} \tag{36}$$

The zero-order SL peak position $\Delta\theta_0$

The expression $(\sum t_j \epsilon_{\perp j})$ for $\Delta\theta_0$ implies that in lattice-matched superlattices such as GaInAs/InP, GaInP/GaAs, ZnSe/GaAs and InSb/CdTe, $\Delta\theta_0$ could be strongly affected by those very thin, but highly-strained (3–10%) interfacial monolayers. Let us take as an example ZnSe/GaAs SL on GaAs(001) with the interfacial Ga_2Se_3 compound. If m monolayers of zinc blende Ga_2Se_3 compounds exist at each interface, then

$$\Delta\theta_0 = -k_\perp \frac{(t_{ZnSe}\epsilon_{\perp ZnSe} + m a_{GaSe}\epsilon_{\perp GaSe})}{(t_{GaAs} + t_{ZnSe} + m a_{GaSe})} \tag{37}$$

The perpendicular mismatch with the GaAs substrate is about 4.8×10^{-3} for a ZnSe layer and roughly -10^{-1} (after the tetragonal distortion) for a Ga_2Se_3 layer [47]. Then for a 100 Å ZnSe/100 Å GaAs SL, $t_{ZnSe}\epsilon_{\perp ZnSe} = 0.48$ Å and $a_{GaSe}\epsilon_{\perp GaSe} = -0.56$ Å. Thus, even a single ML of Ga_2Se_3 at each interface will shift the zero-order peak position from the negative-angle side (without Ga_2Se_3) of the substrate peak, to the positive-angle side (with one ML of Ga_2Se_3). The same situation occurs in a CdTe/InSb SL if an In_2Te_3 interfacial compound is considered. An In_2Te_3 interface in the InSb/CdTe SL has been suggested, based on the observed location of the zero-order SL peak which was at the positive-angle side of the InSb Bragg peak in the X-ray rocking curve. $\Delta\theta_0$ is a negative value if only the InSb and CdTe layers are considered [86].

Let us take the lattice-matched GaInAs/InP SL as a second example to consider the relation between $\Delta\theta_0$ and the detailed interface grading in the group-V sublattice. Consider a 100 Å $Ga_{0.47}In_{0.53}As$/100 Å InP SL with an abrupt interface. If both interfaces are InAs MLs ($\epsilon_\perp = 6.75 \times 10^{-2}$), then $\Delta\theta_0 = -122$ arcsec. If one interface is InAs ML and the other interface is GaInP ML ($\epsilon_\perp = -6.64 \times 10^{-2}$), then $\Delta\theta_0 = +3.4$ arcsec. If both interfaces are GaInP MLs, then $\Delta\theta_0 = +129$ arcsec. This shows an extremely sensitive dependence of $\Delta\theta_0$ on the interfacial molecular layer.

Next consider a graded group-V sublattice and an abrupt group-III sublattice. If at both interfaces As atoms tend to replace P and form InAsP (more transition layers with

a positive $\epsilon_\perp$), then $\Delta\theta_0$ will become more negative. If at both interfaces P atoms tend to replace As and form GaInAsP (more transition layers with negative $\epsilon_\perp$), then $\Delta\theta_0$ will become more positive. If a graded InAsP is formed at one interface and GaInAsP at the other over the same length of scale, then $\Delta\theta_0$ will remain about the same. These examples show the strong effect that the detailed interfacial structure has on the zero-order peak position of lattice-matched SLs. For these SLs, the zero-order peak position $\Delta\theta_0$ is not related to the average composition of SL in a straightforward manner as claimed in the literature [66].

The overall SL peak profile

The envelope function is useful in the SL analysis partly because its intensity profile varies less rapidly with angle than the SL profile I_{SL} itself. Here I discuss the characterization of the interface structure of SL with the help of the envelope function. All simulations were done using the matrix method of the dynamical theory presented in Section 4.2.

Fig. 28 shows a simulated 004 Cu $K\alpha_1$ rocking curve for atomically abrupt interfaces of a 30-period 70 Å $Ga_{0.47}In_{0.53}As$/175 Å InP SL lattice-matched to InP(001): —In-P*-GaIn-As- — -GaIn*-As*-In-P—. Therefore, each period consists of four layers: 1.36 Å GaInP, 68.6 Å GaInAs, 1.57 Å InAs, and 173 Å InP. The calculated SL rocking curve and the envelope function profile (Eq. (36)) are shown. Unless the angular step is very small (of the order of 2–5 arcsec), then the true SL peaks will be easily missed in the calculation and also in the experiment (the step angle in Fig. 28A was 25 arcsec), and thus the SL peak intensity can be estimated more accurately by the intensity of the envelope function at the SL peak position. This point is reinforced by Fig. 28B, where the step angle was 3.75 arcsec and the SL peak intensity is near 10^{-4}, close to the envelope function values in Fig. 28A. This also points to the importance of a small angular step size in the experimental data.

Consider a single transitional group-V atomic plane at each interface: —In-P*-GaIn*-$As_{0.5}P_{0.5}$*-GaIn-As- — -GaIn-As*-In*-$As_{0.5}P_{0.5}$*-In-P—. The 004 Cu $K\alpha_1$ SL peak profiles are affected significantly, as shown in Fig. 29 by the envelope profiles simulated with a coarse step angle (Fig. 29A) and by both the envelope and SL profiles simulated with a fine step angle (Fig. 29B). The magnified view in Fig. 29B clearly shows the significant

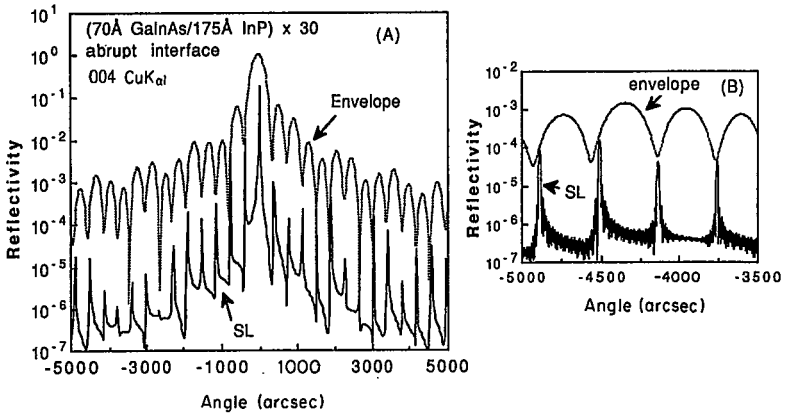

Fig. 28. Simulated 004 Cu $K\alpha_1$ rocking curve for 30-period 70 Å $Ga_{0.47}In_{0.53}As$/175 Å InP SL on an InP(001) substrate. The interfaces are assumed to be atomically abrupt. (A) The angular step in simulation was about 25 arcsec and (B) the step size was 3.75 arcsec.

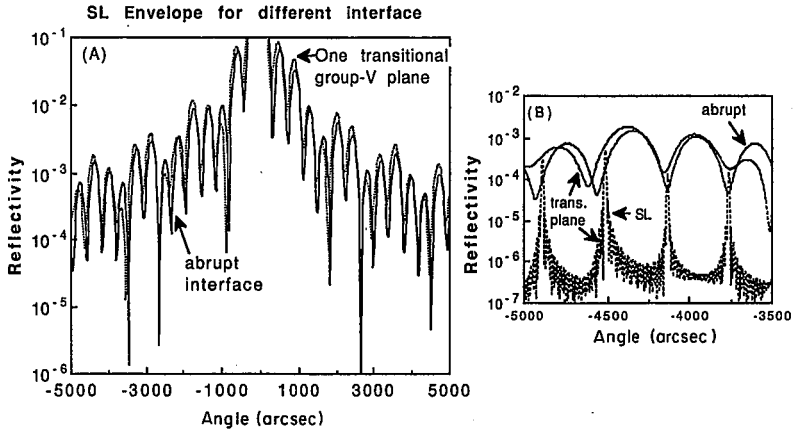

Fig. 29. Envelope profile (A) and both envelope and SL profiles (B) for the same sample as in Fig. 28, comparing two different interfaces: abrupt interface (solid line) and one transitional AsP atomic plane at the interface (dotted line).

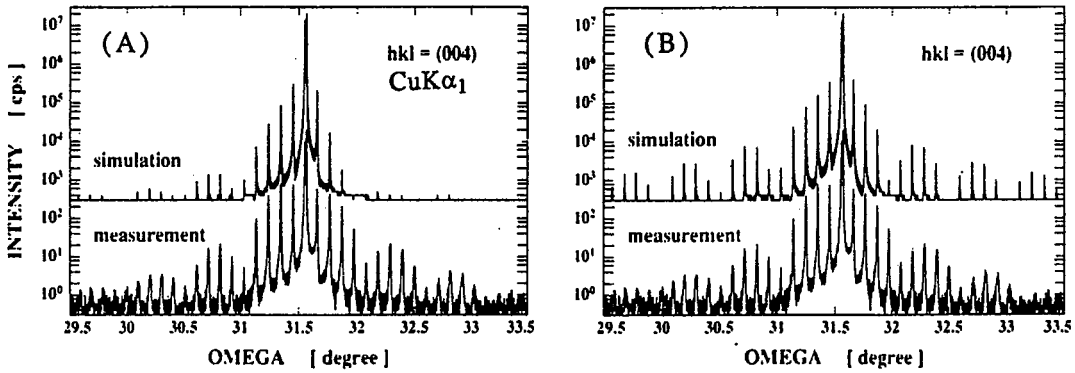

Fig. 30. Experimental and simulated 004 Cu $K\alpha_1$ rocking curves of a 20-period 100 Å $Ga_{0.453}In_{0.547}As$/400 Å InP MQW structure. In (A), the simulation was performed assuming abrupt interfaces, and in (B) after inserting a ML of $GaInAs_{0.5}P_{0.5}$ in the InP→GaInAs interface and a ML of $InAs_{0.5}P_{0.5}$ in the GaInAs→InP interface. Data from Ref. [92].

variation of the SL peaks with an atomic plane variation at the interface. In this case a period consists of six layers: 1.36 Å GaInP, 2.83 Å GaInAsP, 65.8 Å GaInAs, 1.57 Å InAs, 3.04 Å InAsP, and 171 Å InP.

The interface problems in the GaInAs/InP SL system have been investigated by the X-ray rocking-curve analysis by several groups [90–94]. Meyer et al. [92] have considered the strained monolayers for an abrupt interface and the transitional group-V layers for a graded interface. Fig. 30 shows the experimental and simulated 004 Cu $K\alpha_1$ rocking curves of $Ga_{0.453}In_{0.547}As$/InP MQW structure with 20 periods of 100-Å GaInAs and 400-Å InP from Ref. [92]. The simulation in Fig. 30A is assuming abrupt interfaces, and that in Fig. 30B is assuming a monolayer of transitional $GaInAs_{0.5}P_{0.5}$ and a monolayer of $InAs_{0.5}P_{0.5}$ inserted at the lower and upper interfaces of the GaInAs layer, respectively. Clearly a transitional monolayer in the group-V sublattice gives a much better agreement than the abrupt interface does between experiment and simulation, suggesting the carry-over of group-V elements and formation of strained monolayers at the interfaces. MOCVD-grown GaAs/$Ga_{0.504}In_{0.496}P$ MQW samples were analyzed using the rocking curves by Bhat et al. [12].

They report a much better agreement between experiment and simulation if a strained GaInAsP layer 8 Å or 6 Å thick is considered at each interface. These strained layers are perhaps an averaged layer of a graded interface over two or three MLs, because a ML is about 3 Å thick.

In Fig. 31, curve (a) shows experimental 004 rocking curves of a 15-period 670 Å InSb/670 Å CdTe superlattice grown by MBE, originally reported in Ref. [13]. Curves (b) and (c) in Fig. 31 show simulated rocking curves using the dynamical theory; curve (b) with a two-layer period without any interfacial layers and curve (c) with a strained layer 15 Å thick ($\epsilon_\perp = -4\times10^{-2}$) at the InSb→CdTe interface and a layer 20 Å thick ($\epsilon_\perp = 2\times10^{-3}$) at the CdTe→InSb interface. Neither of the simulated curves gives a good agreement with the experimental data. The author reports that all attempts with varying thicknesses and strains failed to produce a good fit to the data [13]. Fig. 32 shows three simulated curves which give a better agreement with the data. In this simulation, the following assumptions were made regarding the interface structure: (i) that the nearest neighbor planes at the interface are between group-V and group-II or between group-III and group-VI elements; (ii) that for a graded interface, the group-III sublattice mixes with group-II sublattice and group V with group VI; (iii) that the interatomic distance equals the sum of Pauling's covalent radii [95,96] of the constituent elements for the Cd-Sb and In-Te molecular planes in the tetrahedral configuration; and (iv) that for the layers of InSb and CdTe, the top atomic plane is a Sb-plane and a Te-plane, respectively.

With these assumptions, a sample with an abrupt interface will have a molecular monolayer of CdSb for the InSb→CdTe interface and a monolayer of InTe for the CdTe→InSb interface. From assumption (iii), an effective lattice constant was taken to be 6.3854 Å for InTe and 6.5705 Å for CdSb. In Fig. 32, only the Cd (and thus In) sublattice is graded at the CdTe→InSb interface, with an abrupt interface for the other sublattice (Te and Sb). Fig. 32 shows the cases where there are two, three and four In_xCd_{1-x} 004 atomic planes with $0<x<1$ and with a linear grading. The simulated curves with three or four InCd atomic planes appear to agree better with the experimental data (Fig. 31, curve (a))

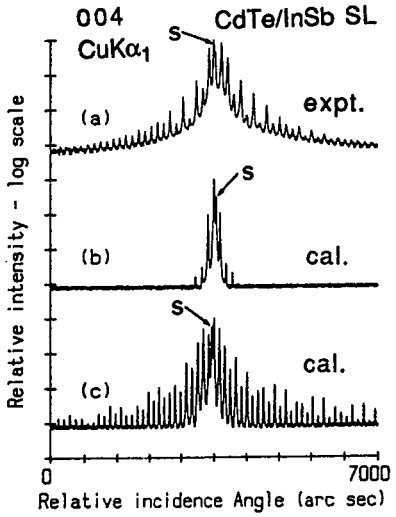

Fig. 31. Experimental (curve (a)) and simulated (curves (b) and (c)) 004 Cu $K\alpha_1$ rocking curves of a 15-period 670 Å InSb/670 Å CdTe superlattice grown by MBE. In curve (b), no strained interfacial plane was assumed and in curve (c) the simulation was done assuming a layer 15 Å thick with $\epsilon_\perp = -4\times10^{-2}$ at the InSb→CdTe interface and a layer 20 Å thick with $\epsilon_\perp = 2\times10^{-3}$ at the CdTe→InSb interface. Data from Ref. [13].

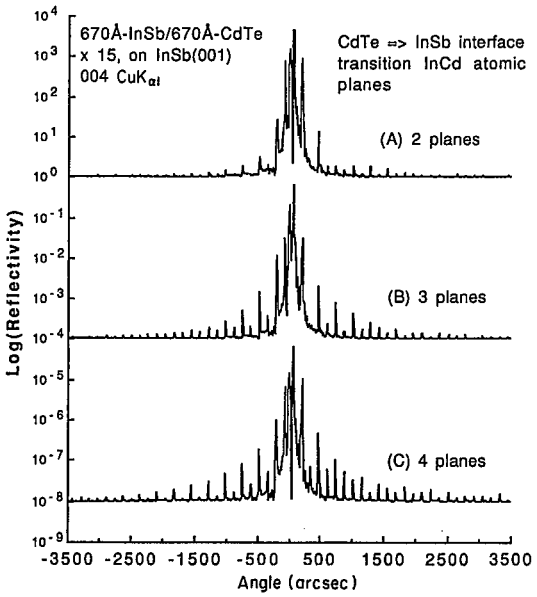

Fig. 32. Simulated 004 rocking curves for the same samples as in Fig. 31. The InSb→CdTe interface was assumed abrupt and the CdTe→InSb interface had two, three or four transitional InCd atomic planes and an abrupt Te-to-Sb sublattice. See text for a detailed discussion.

than either of the simulated curves in Fig. 31. This example attests to the importance of a detailed modeling of interface atomic monolayers in the X-ray rocking-curve analysis. The CdTe/InSb SL, like the ZnSe/GaAs SL, is a very interesting but difficult system for X-ray diffraction analysis because of the other possible interfacial structures such as In_2Te_3, Cd_3Sb_2 and Sb_2Te_3, for which one third of the group-III or group-V zinc blende sublattice must be vacant.

From the experimental and rocking curves in Figs. 31–32, it may be concluded that the appearance of higher-order SL peaks in the experimental data, which is not observed in the simulated rocking curves assuming abrupt interfaces, is an indication of the presence of interfacial atomic planes. With increased numbers of interfacial atomic planes, the higher-order peaks become more clearly visible, as Fig. 32 shows. Comparison between Fig. 31, curve (c), and Fig. 32 shows that the overall profile of the SL peaks is sensitive to the type of interfacial layer, i.e. a single average layer at each interface (Fig. 31, curve (c)) vs. grading over the few atomic planes (Fig. 32). The experimental and simulated curves of Fig. 30B only reinforce this conclusion.

5.2. Analysis of strained quantum-effect device structures

Here I will discuss a few strained quantum-effect device structures analyzed by the X-ray rocking curves.

5.2.1. Strained single quantum-well structure

Eq. (28) and Fig. 24 elucidate the physical principle involved in the X-ray rocking-curve analysis of very thin strained layers. Strain and thickness of a strained quantum well (layer A in Fig. 24) can be found from an analysis of the Bragg peak profile and the profile of Pendellösung fringes of a cladding layer (layer B in Fig. 24). Fig. 33 shows experimental (004 Fe $K\alpha_1$, dots) and simulated (solid) rocking curves for a strained $InP/Ga_{0.2}In_{0.8}P/$

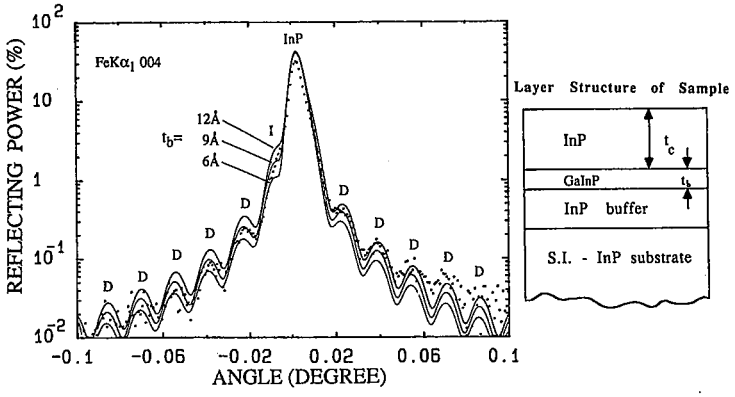

Fig. 33. Experimental and simulated 004 Fe $K\alpha_1$ rocking curves and a schematic of the InP/$Ga_{0.2}In_{0.8}P$/InP(001) sample structure. From the Pendellösung fringe spacing, the InP cladding layer thickness t_c equals 0.47 μm. The simulation fits both the Bragg profile and fringe profile best with $t_b = 9$ Å, the GaInP thickness. Data from Ref. [10].

InP(001) structure [10]. The InP cladding layer thickness was 0.47 μm as determined from the Pendellösung fringe spacing (fringes are marked D in the figure). The fit of the simulated curves to the experimental 004 InP Bragg peak and fringe profile indicates that the GaInP is 9 Å thick, with a better than 3 Å confidence. This is very close to the nominal thickness, which was 10 Å. Tapfer et al. have analyzed a 0.14 μm Si/Ge/Si(001) structure with a Ge layer 3 ML thick, using the X-ray rocking curve [97]. The rocking-curve profile is sensitive to a submonolayer variation in the Ge layer thickness. Note, however, that the X-ray interference analysis can only determine the strain–thickness product as suggested by Eq. (28) and Eq. (29). The thickness can be determined uniquely only if the composition (or strain) is known, or vice versa. In Fig. 33, the GaInP composition was assumed to be the same as the nominal-growth value of 0.2.

5.2.2. *Strained multiple quantum-well structure*

The strained GaInAs/GaAs MQW structure is important as the active layer in high-efficiency laser diodes (emission wavelength, $\lambda = 0.98$ μm) used as the pumping source in an Er-doped optical fiber for optical fiber communication at $\lambda = 1.55$ μm. Fig. 34 shows experimental 004 Cu $K\alpha_1$ rocking curves of MBE-grown 500 Å GaAs/100 Å GaInAs MQW structures on a GaAs(001) substrate, indium composition of 0.16, with different numbers of periods, originally reported by Wang et al. [98]. When the number of periods is equal to or less than six ($N \leqslant 6$) both the principal and secondary SL peaks appear clearly, with the $N-2$ secondary peaks appearing between the principal peaks, symmetrically around the principal peaks. At $N = 7$, the secondary peaks are still observable but appear *asymmetrically* around each principal peak, with a higher intensity at the higher-angle side of each principal peak. They report an observation by Normarski optical microscope of a smooth surface up to six periods and cross-hatched patterns for $N \geqslant 7$ due to the strain relaxation via formation of misfit dislocations [98]. Their critical thickness for strain relaxation, from the X-ray data and optical microscope observation, agreed with the single kink mechanism of the Matthews–Blakeslee model [52].

Note that the strain relaxation can be measured through an angular shift of the Bragg peak with a typical resolution of about 2×10^{-4} in the strain relief, which makes the X-ray measured critical thickness higher than that predicted by the Matthews–Blakeslee model but lower than that predicted by the Peoples–Bean model [54]. Since the critical thickness

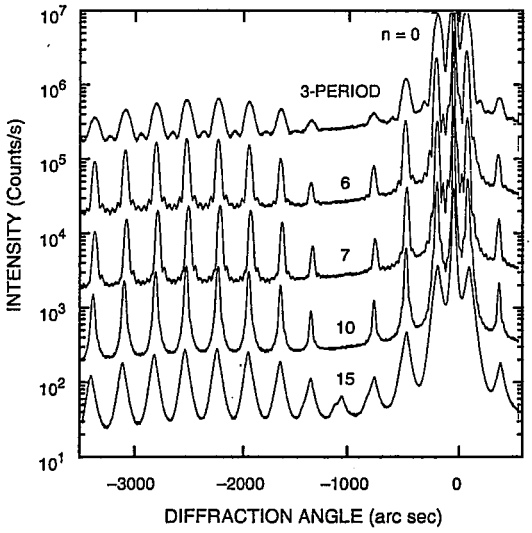

Fig. 34. Experimental 004 Cu $K\alpha_1$ rocking curves of MBE-grown 500 Å GaAs/100 Å $Ga_{0.84}In_{0.16}As$ MQW structures on a GaAs(001) substrate. Strain relaxation starts from 7-period, where the secondary SL fringes begin to appear asymmetrically around each principal SL peak. Data reprinted with permission of MIT Lincoln Laboratory, Lexington, MA [98].

measured via the appearance of the secondary SL peaks agrees with the Matthews–Blakeslee model, the transition from symmetric appearance to an asymmetric appearance of the secondary peaks seems to be a more sensitive measure of the onset of the strain relaxation than the shifting of a Bragg peak (such as the zero-order peak or any principal SL peak). This point can also be argued from the comparison of the zero-order or principal peak positions and the comparison of the appearance of secondary peaks between the rocking curves for $N=6$ and 7 in Fig. 34. As the strain relaxes still further, as in the curves with $N=10$ and 15, the secondary peaks are no longer observable and the principal peaks broaden asymmetrically with more intensity in the right half of the peak. A model simulation of the rocking curves considering a non-uniform strain relaxation (i.e. a non-uniform $\epsilon_{\parallel}$) within the plane of the sample (thus creating localized regions with a lower $\epsilon_{\perp}$) could explain this asymmetric broadening of the principal peaks for $N \geqslant 10$ [99].

5.2.3. Optoelectronic device structures

Fig. 35 shows an MBE-grown resonant tunneling diode (RTD) structure and the measured (dots) and simulated (solid line) rocking curves. This AlAs/GaAs RTD has a strained $Ga_{1-x}In_xAs$ quantum-well layer 50 Å thick acting as a spacer layer in the emitter side. A device measurement showed an improved performance (increased peak current and peak-to-valley ratio) for a higher indium content in the GaInAs layer because a deeper GaInAs spacer well could hold more resonant electrons at the peak voltage [101,102]. Fig. 35(a) shows a good fit to the measured rocking curve by a simulated curve using the nominal-growth parameters. For the five structures investigated ($x=0$, 0.05, 0.1, 0.15, and 0.2), all rocking-curve analyses showed a good agreement with the nominal growth parameter values except for $x=0.15$, whose rocking-curve analysis is shown in Fig. 35(c). Fig. 35(c) shows a best fit with $x=0.13$, with all other layer parameters being the same as in the sample schematic. The electrical data on the static device characteristics also showed an anomalous deviation of the $x=0.15$ sample from the trend of the rest of the samples [101].

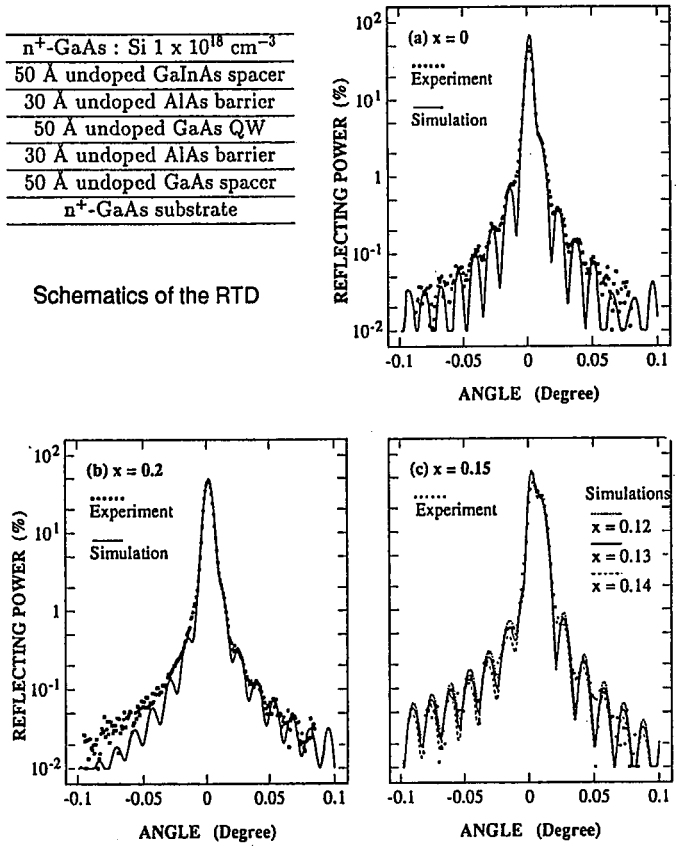

Fig. 35. Layer schematic and the experimental and simulated 004 Fe $K\alpha_1$ rocking curves of a resonant tunneling diode grown on GaAs(001). The X-ray analysis result agreed well with the device data. Data from Ref. [100].

Other device structures with a strained quantum well or barrier layer can also be analyzed by X-ray rocking-curve measurement and simulation. Examples of such device structures are a strained AlGaAs/GaInAs/GaAs quantum-well laser diode [103], a modulation-doped field-effect transistor (MODFET) such as 430 Å InAlAs/AlAs/InAs/InGaAs/InP(001) with a strained spacer (AlAs) and channel (InAs) layer [104], and a 0.25 μm-n-GaAs/GaInP/p-GaAs/n-GaAs heterojunction bipolar transistor (HBT) with a GaInP hole-blocking layer [105]. A rocking-curve simulation using the matrix method of the dynamical diffraction theory, presented in Section 4.2, showed a clear change in the 004 Bragg profile when the thin active layer was varied in the QW-laser (GaInAs), MODFET (InAs) and HBT (GaInP) [11,106]. Figs. 36 and 37 show the sample structure and the simulated rocking curves for a QW laser diode [11] and a MODFET structure, respectively. With the changing thickness of an active layer (quantum well or barrier) in the device, the rocking-curve profile shows a clearly distinguishable difference. In Fig. 36, the interference structure within the 004 Bragg peak of the $Al_{0.4}Ga_{0.6}As$ cladding layer is the measure, and in Fig. 37 the Bragg peak tail and the Pendellösung fringe profile are the measure of the layer parameter. The Pendellösung fringe profiles in Fig. 37 appear at a reflectivity between 10^{-6} and 10^{-4} and thus a detector with low background noise and enhanced dynamic range may be needed for the measurement.

0.1 μm	GaAs	cap layer
0.2 μm	$Al_xGa_{1-x}As$	$x = 0.4 \rightarrow 0$
1.5 μm	$Al_{0.4}Ga_{0.6}As$	cladding layer
0.2 μm	$Al_xGa_{1-x}As$	$x = 0 \rightarrow 0.4$
100 Å	GaAs	
t_a	$Ga_{0.63}In_{0.37}As$	active layer
100 Å	GaAs	
0.2 μm	$Al_xGa_{1-x}As$	$x = 0.4 \rightarrow 0$
1.5 μm	$Al_{0.4}Ga_{0.6}As$	cladding layer
0.2 μm	$Al_xGa_{1-x}As$	$x = 0 \rightarrow 0.4$
0.5 μm	GaAs	buffer

GaAs (001) substrate

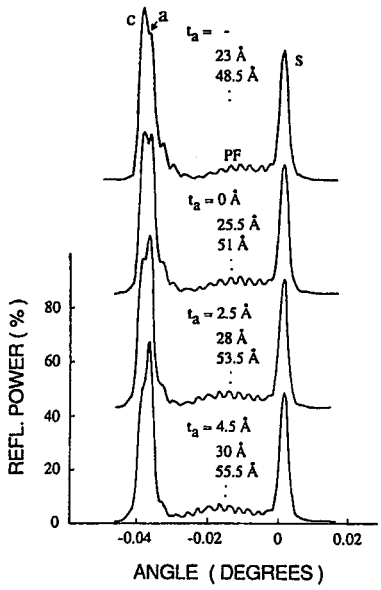

Fig. 36. Layer schematic and the simulated 004 rocking curves of a graded-index separate-confinement quantum-well laser diode. The reflecting power is on a linear scale. The peak marked by c is the AlGaAs cladding-layer Bragg peak and s is the substrate peak [11].

MODFET structure

	50A	$In_{.53}Ga_{.47}As$	
	370A	$In_{.52}Al_{.48}As$	
	60A	$In_{.52}Al_{.48}As$	spacer
t_b	~ 30A	AlAs	barrier
t_c	~ 30A	InAs	channel
	400A	$In_{.53}Ga_{.47}As$	
	4000A	$In_{.52}Al_{.48}As$	buffer

(001) SI InP-sub

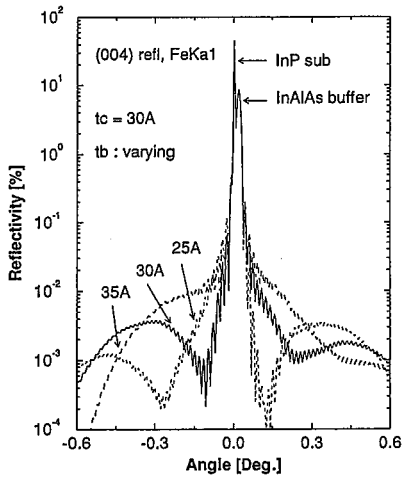

Fig. 37. Layer schematic and the simulated rocking curves of a MODFET device. Note the very low intensity of the fringe profile (reflectivity less than 0.01%).

6. Diffuse scattering of defects in semiconductors

HRXRD techniques are increasingly applied towards defect characterization in semiconductor crystals. By using diffuse scattering, defects investigated include spherical clusters of point defects, dislocation loops and stacking faults with typical defect sizes ranging from 0.1 to 6.0 μm in radius. Diffuse scattering caused by very small defects (radius < 10 Å) can be investigated using a single-crystal diffractometer (SCD) [15]. Larger defects require a higher angular resolution and therefore the HRXRD techniques (DCD and TCD) must be used. Here, I will discuss the analysis of diffuse scattering in the Bragg diffraction

geometry. The diffuse scattering measurement near the critical angle of total reflection (small-angle scattering) is beyond the scope of this review.

6.1. Theory of diffuse X-ray scattering

Theoretical work on diffuse X-ray scattering by deformed crystals was begun in the mid-1940s by Eckstein [107] and Huang [108], followed among others by Krivoglaz [17], Dederichs [16,15], Trinkaus [19,109], Larson [18,110,111], Kato [112] in the 1960s and 70s, and more recently by Holy [20,113] and others [114,115]. A kinematical theory of diffuse scattering consists in the ensemble averaging of the structure factor considering randomly distributed micro-defects. The theory gives a distribution of scattered intensity in the reciprocal space near a reciprocal lattice point. Kato [112] and Holy [113] generalized the Takagi–Taupin equation allowing for defects uniformly distributed over the volume, and developed a statistical-dynamical theory of diffraction in imperfect crystals. Kato's theory describes the intensity integrated over all angles, but Holy considered the angular profiles of diffuse scattering by solving the Takagi–Taupin equation in a Green's-function approach and determined the so-called mutual coherence function of the deformation fields by averaging over a statistical ensemble of randomly distributed defects. The dynamical theory for the angular profile of diffuse scattering is rather complicated, and a kinematical approximation has been of more practical use [17,15,113]. Available theories for diffuse scattering, however, are appropriate only for bulk samples with uniformly distributed defects. A theory is still needed for diffuse scattering for samples with a depth-dependent non-uniformity such as thermally-diffused crystals, ion-implanted crystals [116], surface-polished semiconductor crystals [117,23], semiconductor heterostructures [22], and superlattices. Here, I will first introduce an approach which could serve such a purpose in the depth-dependent structures and is analogous to the X-ray rocking-curve theory [118].

If the deformation term is neglected or if the strain field is constant, then an analytical solution to the Takagi–Taupin equation can be found. Using this analytical solution for the incident field $\mathbf{D}_0(z)$, the reflected wave amplitude, $\mathbf{D}_h$, can be obtained by integrating the second equation (for D_h) of the T–T equation, Eq. (12). For a bulk crystal or for a crystal plate with a constant strain, this gives the following scattering amplitude, $X = D_h/D_0\sqrt{|b|}$:

$$X(\xi) = i\sigma' B \int_0^{-\infty} ds_h \exp[i\sigma'(C-S)s_h] \exp(i2\pi \mathbf{h}\cdot\mathbf{u}) \tag{38}$$

where ξ is a coordinate axis parallel to the crystal surface (i.e. the x axis of Fig. 8), σ' is $\sigma/\sqrt{|b|}$, $\mathbf{u}$ is the deformation field inside the crystal medium, s_h is the coordinate axis parallel to the diffracted wave vector $\mathbf{k}$ inside the medium, and $\mathbf{h}$ is the reciprocal lattice vector of the undisturbed crystal lattice. Other parameters, σ, B, C and S have been defined in Eqs. (16) and (17). Note that when the crystal is perfect ($\mathbf{u}=0$), Eq. (38) reduces to the dynamical diffraction amplitude of the substrate, Eq. (18). First a few comments on this formula: (i) this is essentially a semi-kinematical approximation where the undisturbed part of the lattice is treated in the dynamical theory and the defect deformation field is treated in kinematical approximation; (ii) the normal absorption and extinction effects are taken into account through the $\exp[i\sigma'(C-S)s_h]$ term. Fig. 38 shows a plot of $C-S$ vs. the incident

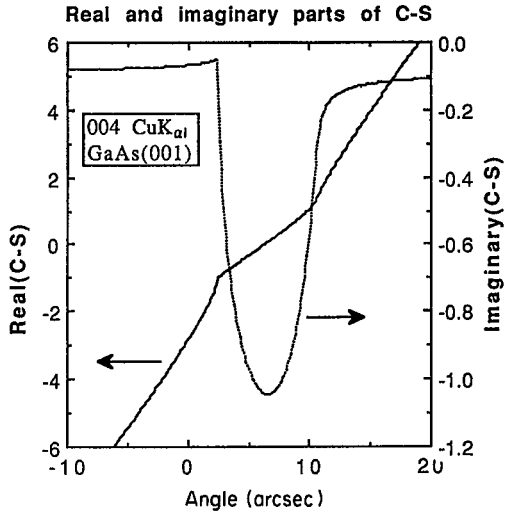

Fig. 38. Plot of the real and imaginary parts of $C-S$ of Eq. (38) as a function of the incident angle. The imaginary part is the measure of X-ray penetration depth. The y-axes values must be multiplied by $\pi\sqrt{\gamma_0|\gamma_h|}/\lambda\sigma$ to obtain the correct values and units.

angle $\Delta\theta$ for a 004 Cu Kα reflection in a GaAs(001) crystal. Here, the angular profile of Im$(C-S)$ may be convolved with a gaussian broadening function to account for possibly a broader Bragg peak in the real crystal; (iii) an additional absorption loss associated with the diffuse scattering (static Debye–Waller factor) can be added to the Im$(C-S)$ term [16]; and (iv) the Bragg peak position in the reciprocal lattice space may be shifted due to an expanded 'average' lattice, and this can be accommodated through an adjustment to the reciprocal lattice vector **h**, similar to the approach taken by Dederichs [16].

This formula may be used in simulating the topographic image of a defect represented by the deformation field, **u**(**r**), in a semikinematical approximation. The formula (Eq. (38)) provides a much simplified way of simulating the topograph compared with the approach taken by Riglet et al. [119]. They numerically integrated the T–T equation to simulate the topographs of two types of 60° misfit dislocations in a heterostructure. Fig. 39 shows a simulated topographic image using Eq. (38) for a 60° dislocation in bulk GaAs(001), where the dislocation line runs parallel to the surface and normal to the diffraction plane at 1.3 μm below the surface with a (111)[011] slip system. The figure also shows the intensity profile corresponding to the image, and in the inset the incident angle is indicated. Using Eq. (38) for the simulation, only one coordinate axis (s_h) which runs parallel to the diffracted wave vector needs to be considered, making the simulation greatly simplified and flexible, as compared with the need to consider both the incident and diffracted wave vectors (a mesh) of Riglet et al. [119].

The diffuse scattering amplitude is then given by Eq. (38) with the exp(i2π**h**·**u**) term replaced by [exp(i2π**h**·**u**) − 1] where the unity subtracted is the coherent, Bragg-diffraction part. The imaginary part of $C-S$ is the absorption/extinction factor (in Fig. 38, the zero angle corresponds to an unmodified Bragg angle θ_B given by $2d \sin\theta_B = \lambda$). The extinction of X-ray will strongly affect the diffuse intensity profile only for the Ewald sphere which passes very close to the q-space origin (note that it coincides with the analyzer CTR if a single-reflection analyzer is used). The diffuse scattering amplitude can then be written as

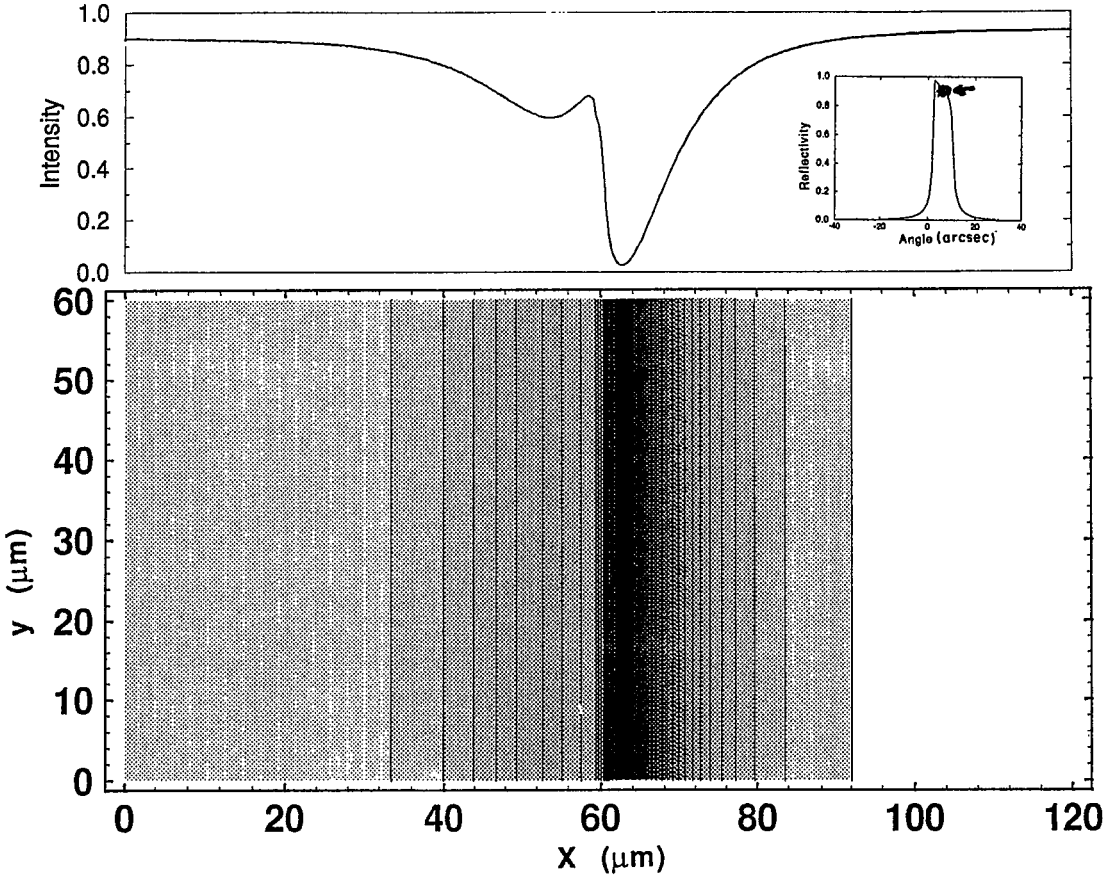

Fig. 39. Topographic image simulated using Eq. (38) for a 60° dislocation in a bulk GaAs(001). The dislocation line runs parallel to the surface and normal to the diffraction plane at 1.3 μm below the surface with a (111)[011] slip system. An intensity profile across the surface and the incident angle are also shown.

$$X_s(\mathbf{q}) = -\mathrm{i}\int_{-\infty}^{\infty} \mathrm{d}x \int_{-\infty}^{\infty} \mathrm{d}y \int_{0}^{-\infty} \mathrm{d}z \sigma' B \exp(\mathrm{i}2\pi\mathbf{q}\cdot\mathbf{r})[\exp(\mathrm{i}2\pi\mathbf{h}\cdot\mathbf{u}) - 1] \exp(2\pi\kappa_i z) \tag{39}$$

where

$$\kappa_i = K(\lambda\sigma/\pi)(C-S)_i/2\sqrt{\gamma_0|\gamma_h|} + \text{static Debye–Waller term} \tag{40}$$

Here, $(C-S)_i$ is the imaginary part of $C-S$ (see Eq. (17) and Fig. 38), and the static Debye–Waller term is included to account for the additional absorption caused by the diffuse scattering. As shown in Fig. 8, the x axis is parallel to the sample surface, the y axis is normal to the diffraction plane (the zx plane), and the z axis is parallel to the outward surface normal. The last exponential term shows that deeper regions will contribute less to the diffuse scattering owing to absorption and extinction. The factor $\exp(2\pi\kappa_i z)$ in the integrand may be omitted if the crystal has a defect distribution that is uniform in depth. A three-dimensional distribution of the diffuse scattered intensity near a reciprocal lattice point $\mathbf{h}$ is then

$$J(\mathbf{q}) = |X_s(\mathbf{q})|^2 \text{ for 3D distribution in the } q \text{ space} \tag{41}$$

Table 4
The diffraction modes and their experimental and theoretical characteristics: the single-crystal diffraction (SCD) is for very small defects

Mode	Integral of $J(\mathbf{q})$	Differ. angle	Resolution	Range	Defect size
SCD	$\int dq_0\, dq_E\, dq_y \delta(q_y)$	none	0.1°	5°	<20 Å
DCD	$\int dq_0\, dq_y$	$\Delta\theta$	2–6 arcsec	0.5°–5°	50 Å–20 μm
TCD	$\int dq_y$	$\Delta\theta$, $\Delta\omega$	2–5 arcsec	400 arcsec	50 Å–20 μm

Total scattering intensity equals $J(\mathbf{q})$ plus the coherent, Bragg diffraction. In the range of $\mathbf{q}$ vectors (or in the angular range) where the diffuse-scattered intensity $J(\mathbf{q})$ is examined, the Bragg intensity of the coherent lattice is usually small and is assumed to be negligible. To obtain the TCD and DCD diffuse intensity from $J(\mathbf{q})$, the following integrations must be performed:

$$I_{TCD}(q_1, q_2) = \int dq_y\, J(\mathbf{q}) \qquad \text{for TCD} \tag{42}$$

$$I_{DCD}(q_0) = \int dq_y\, dq_E\, J(\mathbf{q}) \qquad \text{for DCD} \tag{43}$$

where q_y is perpendicular to the diffraction plane (i.e. vertical direction), and q_0 is perpendicular to the Ewald sphere (parallel to the diffracted wave vector) as defined in Fig. 8. $I_{TCD}(q_1, q_2)$ and $I_{DCD}(q_0)$ may be convolved with the instrumental functions (monochro-collimator and analyzer). Table 4 summarizes the types of diffraction measurements and measurable defect sizes.

6.2. *Analysis of diffuse scattering data*

Here I shall discuss the diffuse-scattering studies of uniform *bulk* semiconductor crystals, because theoretical analysis is available only for uniform bulk samples. The deformation fields outside the defect core, of radius R_d, give rise to Huang diffuse scattering within a corresponding angular range $\Delta\theta < 1/hR_d$, and the deformation fields within the defect core give rise to the so called Stokes–Wilson (S–W) scattering in an angular range $\Delta\theta > 1/hR_d$ where h is the magnitude of the reciprocal lattice vector $\mathbf{h}$ [17,120]. Most analyses of the experimental data [20,21,121–124] were done using the kinematical theories developed by Dederichs and Krivoglaz, and using the defect calculations by Trinkaus [19,109] and Larson [18,110,111]. The theoretical formulas discussed in this paper are therefore based on the kinematical diffuse-scattering theory.

Based on the theory by Krivoglaz [17], Morozov and Bublik [122] summarized the radial intensity profile formulas for dislocation loops and spherical defect clusters. These formulas are:

$$J(\mathbf{q}) \propto \begin{cases} q^{-2} & \text{for } qR_d < x_0 \quad \text{(Huang)} \\ q^{-4} & \text{for } x_0 < qR_d < x_1 \\ q^{-5} & \text{for } x_1 < qR_d \quad \text{(Stokes–Wilson)} \end{cases} \tag{44}$$

for *dislocation loops* where b is the Burgers vector, R_d is the loop radius, $x_0 = \pi/\sqrt{hb}$ and $x_1 = hb$, and

$$J(\mathbf{q}) = A \begin{cases} q^{-2} & \text{for } qR_d < 1 \quad \text{(Huang)} \\ q^{-4} & \text{for } qR_d > 1 \quad \text{(Stokes–Wilson)} \end{cases} \tag{45}$$

for *spherical defect clusters*, where R_d is the cluster radius. For both types of defects, the detailed proportionality constants may be found in Ref. [122].

6.2.1. Triple-crystal diffraction

Isointensity contour

Fig. 40 shows the measured and calculated isointensity contours of diffuse scattering in a GaAs(111) crystal doped with Si impurities, reported by Charnity et al. [125]. The data were measured by a triple-crystal (+ − +) diffractometer. The symmetric part of the measured intensity (Fig. 40(b)) was obtained from the measured data (Fig. 40(a)) using $I_{TCD}^{s}(\mathbf{q}) = 0.5[I_{TCD}(\mathbf{q}) + I_{TCD}(-\mathbf{q})]$. Measured isointensity contours are shifted toward positive q_1 (or q_z), indicating that the average lattice spacing has shrunk slightly. Therefore, the defects must be of vacancy type (the original authors ascribed the positive q_1-shifting to the interstitial-type defects). The simulated isointensity contours Figs. 40(c)–40(f) were obtained by integrating over a vertical beam divergence of $\pm 0.9°$ (or ± 0.02 Å^{-1} in q_y). The authors report that the $\mathbf{b} = \frac{1}{2}\langle 110\rangle$ dislocation loops lying in {111} (Fig. 40(e)) or in {110} (Fig. 40(f)) give good agreements with the experiment (Fig. 40(b)) [125]. The authors,

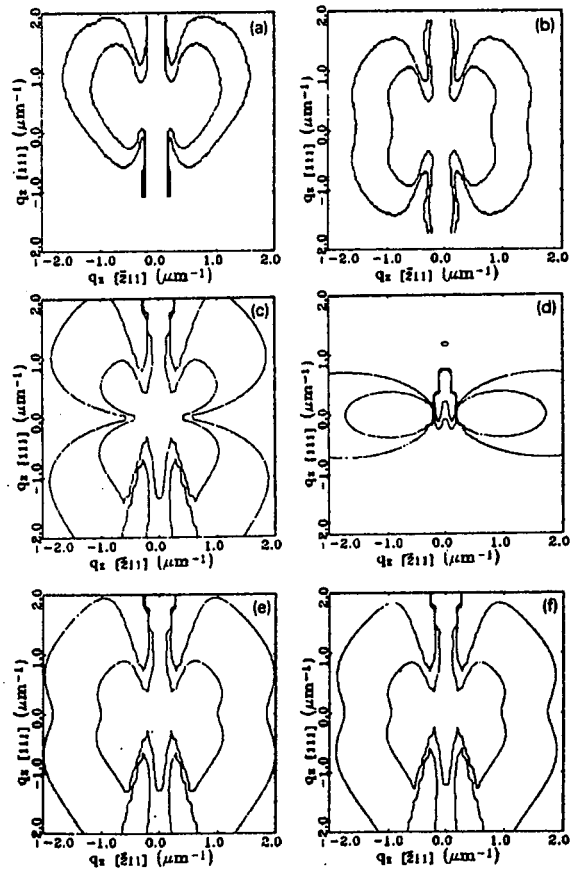

Fig. 40. Isointensity contours around reciprocal lattice point 111 in $(01\bar{1})$ plane of a GaAs(111) crystal doped with Si impurities: (a) as measured in the experiment; (b) symmetrical part of the measured intensity; (c)–(e) calculated isointensity contours for dislocation loops in {111} planes and having a Burgers vector ((c), $\mathbf{b} = \frac{1}{3}\langle 111\rangle$; (d), $\mathbf{b} = \frac{1}{2}\langle \bar{1}10\rangle$; (e), $\mathbf{b} = \frac{1}{2}\langle 110\rangle$); (f) dislocation loops in {110} and $\mathbf{b} = \frac{1}{2\sqrt{2}}\langle 110\rangle$. Neighboring isolines differ by a factor of two in intensity. Data from Ref. [125].

however, appear not to have removed the background (such as thermal) and instrumental (MC and analyzer CTRs in a (+ − +) triple-crystal diffractometer, see Fig. 5) diffuse scattering from their measured data. Therefore, care must be taken in interpreting the data, because the observed anisotropy in Fig. 40(b) could also be associated with the MC and analyzer CTRs (see Fig. 5) superimposed on isotropic diffuse scattering data. The radial intensity distribution from the same samples will be discussed below (in Fig. 43). The dislocation loops and spherical defects in InP and in Cu have been studied using the isointensity contour maps [121,111].

TCD radial intensity profile, $I_{TCD}(q)$

The radial intensity distribution of diffuse scattering $I_{\mathrm{TCD}}(\mathbf{q})$, obtained along a particular **q**-direction in the diffraction plane (see Fig. 6), can show a different q-dependence depending upon whether the angular spread of diffuse scattering in vertical direction is smaller or larger than the vertical acceptance angle of the detector. For very small defects, where the angular spread of diffuse scattering is much larger than the vertical acceptance angle, the result of vertical integration, $\int dq_y$, may be approximated to the value at the diffraction plane, $q_y=0$: $\int dq_y J(q_x, q_y, q_z) \approx J(q_x, 0, q_z)$. Therefore, the Huang diffuse scattering for small defects has the same radial intensity distribution (q^{-2}) as CTRs (see Fig. 4). For large defects, however, the vertical integration $\int dq_y$ gives $I_{\mathrm{TCD}} \propto q^{-m+1}$ for $J \propto q^{-m}$ of Eqs. (44) and (45). For large spherical defects, $I_{\mathrm{TCD}} \propto q^{-1}$ for Huang diffuse scattering and $I_{\mathrm{TCD}} \propto q^{-3}$ for S–W diffuse scattering, and the knee point in the plot $\ln(I_{\mathrm{TCD}})$ vs. $\ln(q)$ gives the defect size R_d. For defects smaller than about 250 Å in radius, Dederichs interpreted the diffuse-scattering profile neglecting the vertical integral [15]. In a Si(111) crystal, uniformly implanted with hydrogen by a multiple energy-implantation technique, Beaufort [124] measured the TCD radial intensity profiles of diffuse scattering near the 440 Bragg reflection along three different **q**-directions: [110], [001] and [112]. These measurements could provide information on the symmetry of the defects through determination of the π^1, π^2 and π^3 coefficients [15]. Fig. 41 shows a TCD radial intensity profile with a q^{-2} dependence for Huang regime

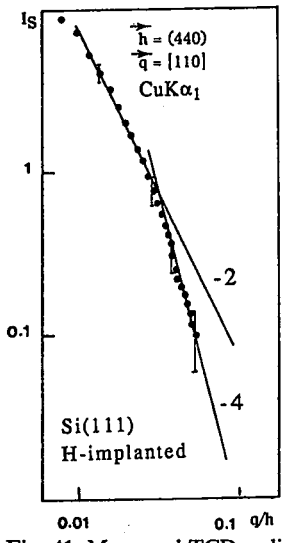

Fig. 41. Measured TCD radial intensity profile for a Si(111) crystal uniformly ion-implanted with hydrogen. The slopes of −2 (Huang) and −4 (Stokes–Wilson) indicate that the defects are clusters of point defects. The knee point gives the defect size approximately 5–9 Å in radius. Data from Ref. [124].

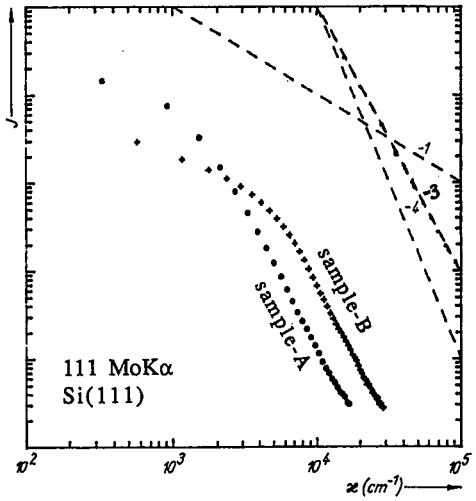

Fig. 42. Measured TCD radial intensity profile along the q_2 axis for a Si(111) crystal heat-treated under two different conditions. Both samples show slopes of -1 (Huang) and -4. The etch pit analysis, TCD isointensity contour data and DCD diffuse intensity profile indicate that the defects are stacking faults in sample A and spherical clusters in sample B. Data from Ref. [20].

and a q^{-4} dependence for S–W regime [124]. In the Huang scattering regime, the influence of CTR on diffuse intensity profile was negligible. The size of the defect clusters was 5–9 Å from the knee point in the curve of Fig. 41.

Holy and Kubena [20] analyzed a Si(111) crystal having 9.8×10^{17} cm^{-3} oxygen impurities. The sample was heat-treated under two different conditions: sample A was annealed at 750 °C for 5 h and then at 1050 °C for 20 h; and sample B was annealed at 750 °C for 40 h and then at 1050 °C for 20 h. Based on etch pit density and X-ray diffuse-scattering analyses, using both TCD and DCD, the defects dominant in sample A were stacking faults of about 6 μm radius and 8×10^7 cm^{-3} concentration, and in sample B they were spherical clusters of about 0.7 μm and 10^{11} cm^{-3} in size and concentration, respectively. Fig. 42 shows their TCD profile measured in the q_2 direction (see Figs. 5–8). It is reported that the slope is -1 in Huang regime, and -4 outside Huang regime (slopes in their plot, however, appear closer to -0.5 and -3 than to -1 and -4). Defect size from the knee point was about 5 μm for sample A and 0.8 μm for sample B. It should, however, be pointed out that the -4 slope in their data for Stokes–Wilson scattering is inconsistent with Eq. (45) for spherical clusters, because the vertical integration should yield -3.

Comments on the possible effect of CTR on interpretation of diffuse scattering

If the diffuse scattered intensity is comparable to or smaller than the intensity of crystal truncation rod, then the Huang diffuse profile taken along a **q**-direction close to a CTR would give a slope more negative than -1 because of the influence from CTR on measured intensity. Fig. 43 illustrates this point for the same GaAs(111) sample as in Fig. 40. In a $(+-+)$ TCD measurement, all three CTRs are expected to be present (see Fig. 5), and in the case of a symmetric Bragg reflection, the analyzer CTR and the collimator CTR are at an angle θ_B (the sample Bragg angle) on either side of the sample CTR ($\theta_B=13.65°$ for 111 Bragg reflection). As the radial scan direction gets closer to a CTR direction (i.e. with increasing ψ, see Fig. 6), the slope of the Huang scattering becomes increasingly negative, as shown in Fig. 43 for $q<2$ μm^{-1}. Taken from a region of the sample surface

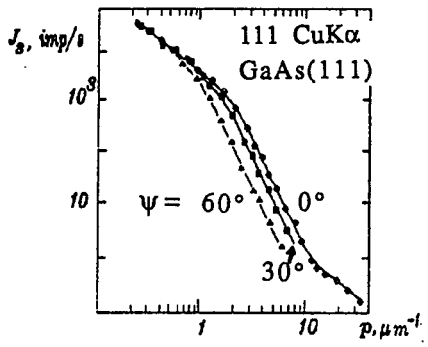

Fig. 43. Radial intensity distribution from a (+ − +) TCD measurement for the same sample as in Fig. 40. With increasing ψ (see Fig. 6), the slope of the Huang scattering region ($p<2$ μm^{-1}) becomes more negative.

where a high density of etch pits was observed, Fig. 43 shows a Huang region ($I_{TCD} \propto q^{-1}$) and a Stokes–Wilson region ($I_{TCD} \propto q^{-3}$). These slopes (-1 and -3) of the radial intensity distribution seem to suggest defect clusters rather than dislocation loops, based on the vertical integration of Eq. (45). At a still larger q (more than 20 μm^{-1}), the $I_{TCD} \propto q^{-1}$ dependence is due to the thermal diffuse scattering [125]. The knee point between the Huang region and the S–W region gives an approximate defect size of 0.5 μm. Therefore, when the diffuse-scattering intensity is weak, a comparative study such as measuring the diffuse scattering before and after processing or comparing the data from the sample with data from a reference crystal is recommended in order to avoid influence from CTRs.

6.2.2. DCD diffuse intensity profile, $I_{DCD}(q_0)$

Integration over the tangent plane to the Ewald sphere, $\int dq_y\, dq_E$, yields

$$I_{DCD}(q_0) \propto \begin{cases} -\ln(q_0) & \text{for } q_0 R_d < x_0 \quad \text{(Huang)} \\ q_0^{-2} & \text{for } x_0 < q_0 R_d < x_1 \quad \text{(Stokes–Wilson)} \\ q_0^{-3} & \text{for } x_1 < q_0 R_d \quad \text{(Stokes–Wilson)} \end{cases} \tag{46}$$

for *dislocation loops*, and

$$I_{DCD}(q_0) \propto \begin{cases} -\ln(q_0 & \text{for } q_0 R_d < 1 \quad \text{(Huang)} \\ q_0^{-2} & \text{for } q_0 R_d > 1 \quad \text{(Stokes–Wilson)} \end{cases} \tag{47}$$

for *spherical clusters*. If the CTR intensity is higher than the Huang diffuse intensity, then the profile would be proportional to q_0^{-2} instead of $-\ln(q_0)$ for small q_0.

Morozov and Bublik [122] studied the diffuse scattering using DCD in a GaAs crystal doped with Si impurities to different concentrations. They removed the thermal diffuse scattering and the effect of the first crystal and sample CTRs by subtracting the rocking-curve data of a reference Ge crystal from the measured data. Fig. 44 shows their result. For a conduction electron concentration $n = 1.1 \times 10^{18}$ (sample 1) or 2.2×10^{18} cm^{-3} (sample 2), only a q_0^{-2} dependence was observed, and they concluded that dominant defects are the defect clusters gathered in clouds of a typical size of 0.1–0.4 μm. For $n = 4.8 \times 10^{18}$ cm^{-3} (sample 3), both q_0^{-2} and q_0^{-3} dependences were observed, as the middle curve in the figure shows, and they ascribed these dependences to the dislocation loops having a typical size of 0.5 μm as measured from the knee point. Not discussed in their paper are the absence of the $I_{DCD} \propto -\ln(\Delta\theta)$ at small $\Delta\theta$ and the relative intensities of CTRs and Huang diffuse scattering.

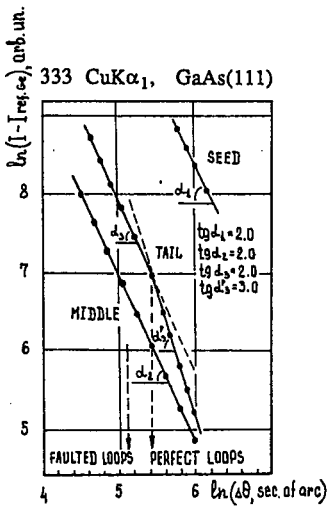

Fig. 44. DCD rocking-curve profile of a GaAs(111) crystal doped with silicon to different concentrations. Data for a reference Ge crystal were subtracted from the measured data. Sample 1 is with conduction electron concentration of $n=1.1\times10^{18}$, sample 2 with $n=2.2\times10^{18}$ cm^{-3}, and both show only a q_0^{-2} dependence, indicating defect clusters with a size of 0.1–0.4 μm. Sample 3 is with $n=4.8\times10^{18}$ cm^{-3}, and shows q_0^{-2} and q_0^{-3} dependence, indicating dislocation loops with the knee point giving 0.5 μm for their size. Sample numbers correspond to the subscript number of angle α. Data from Ref. [122].

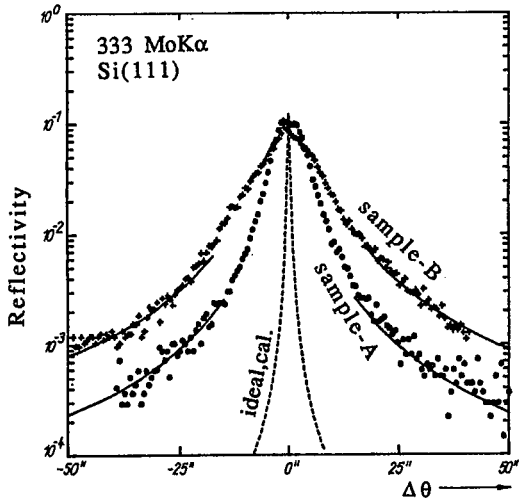

Fig. 45. DCD rocking-curve profiles for the same Si(111) samples as in Fig. 42. The solid curves for large $\Delta\theta$ are the best fits with a theoretical formula (constant times $\Delta\theta^{-2}$), which give a defect concentration of roughly 8×10^{7} cm^{-3} in sample A and 1.7×10^{11} cm^{-3} in sample B. Data from Ref. [20].

Fig. 45 shows the DCD rocking-curve profiles from the same Si(111) samples as Fig. 42 [20]. These data show a $(\Delta\theta)^{-2}$ dependence for large q_0 (or large $\Delta\theta$). The solid lines for large $\Delta\theta$ in the figure are fits with a theoretical formula from which the defect density was estimated. The defect density thus estimated agreed reasonably well with the results of etch pit and TCD profile analyses [20]. The authors also presented three different analyses of the DCD profile [20]: fitting the whole curve (defect size, concentration and strength), linear extrapolation in the Huang region (size), and fitting with constant times $\Delta\theta^{-2}$ for large $\Delta\theta$ (concentration).

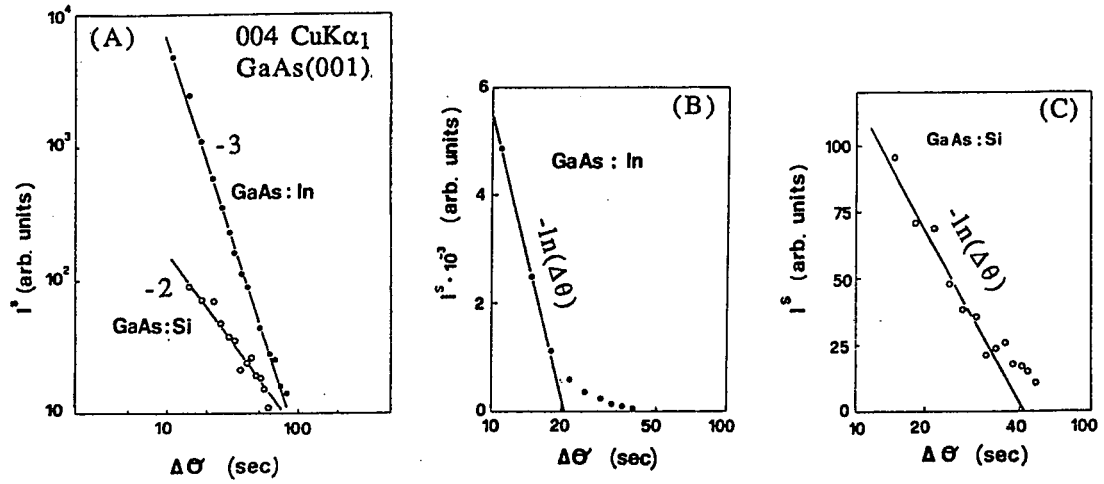

Fig. 46. DCD diffuse-scattering data in GaAs doped with Si or In or undoped, showing $-\ln(\Delta\theta)$ for small $\Delta\theta$ and $(\Delta\theta)^{-m}$ for large $\Delta\theta$. In GaAs:In, $m=3$ indicates dislocation loops, and in GaAs:Si $m=2$ indicates clusters of point defects. From the intercept of the abscissa in (B) and (C), the defect radius is about 0.32 μm in GaAs:In and 0.18 μm in GaAs:Si, and 0.19 μm in undoped GaAs (data not shown). Data from Ref. [126].

Franzosi analyzed the DCD diffuse scattering in bulk GaAs crystals, doped with Si or In impurities or undoped, grown by LEC [126]. Using high-quality Ge crystal data as the reference and subtracting the reference data from the measured data to adjust for thermal diffuse and other background scattering, the symmetrical part of the diffuse scattering was obtained and analyzed: $I^s(\Delta\theta)=0.5[I_{DCD}(\Delta\theta)+I_{DCD}(-\Delta\theta)]-I_{DCD}{}^{Ge}(\Delta\theta)$. Fig. 46 shows log–log and log–linear plots of the GaAs:In and GaAs:Si data. All samples showed that $I^s \propto -\ln(\Delta\theta)$ for small $\Delta\theta$ and $I^s \propto (\Delta\theta)^{-m}$ for large $\Delta\theta$. It was interpreted that at large $\Delta\theta$, $m=3$ means dislocation loops (in the In-doped and undoped samples) and $m=2$ means clusters of point defects (in the Si-doped sample). From the intercept of abscissa in the I^s vs. $\ln(\Delta\theta)$ plots (Fig. 46B and 46C), Franzosi estimates the defect radius to be about 0.18 μm in the Si-doped sample (cluster), 0.32 μm in the In-doped sample (dislocation loop), and 0.19 μm in the undoped sample (dislocation loop) [126].

6.3. TCD measurement of depth non-uniform samples

Experimental TCD isointensity contours and radial intensity profiles were studied in heterostructures by Fewster [22], surface-polished GaAs crystals by Matyi [23], surface-damaged Si crystals by Iida and Kohra [117], and ion-implanted Si crystals by Zaumseil and Winter [116]. No theoretical analysis of the TCD data has been performed in these samples. The application of TCD to these structures has been mostly qualitative, but TCD can serve as a useful quality control tool for semiconductor processing techniques.

The TCD radial intensity profile could serve as an additional tool for the characterization of interfacial roughness in heterostructures. This could complement the double-crystal rocking-curve technique using the CTR method (see Section 5.1.1). In DCD rocking-curve profiles, the crystal truncation rod forms a (local) envelope function to the thickness fringe peaks of a heteroepitaxial layer, and the CTR is due to coherent diffuse scattering by the laterally averaged grading of interface. The contribution of incoherent diffuse scattering in the rocking-curve profile is difficult to determine. The interfacial roughness in the form of terraces could be considered in terms of lateral size fluctuation and height fluctuation.

In TCD radial intensity profiles, the lateral fluctuation of the interface structure will contribute to an incoherent diffuse profile along the q_x direction (transverse scan), while the height fluctuation may contribute to an incoherent diffuse profile along the q_z direction (longitudinal scan). The interface roughness in SiGe/Si has been investigated by a small-angle X-ray scattering technique near the critical angle of total reflection ($\approx 0.5°$) and a resolution on the order of 2 Å on the interfacial roughness was reported [127]. The small-angle, diffuse X-ray scattering data can be analyzed using the kinematical scattering theory in the Born approximation, developed by Sinha [128,129]. An equivalent theory for the interface analysis needs to be developed for the analysis of diffuse scattering measured in a Bragg diffraction mode.

6.4. Conclusion

Studies of defects in semiconductors using the diffuse-scattering analysis are a relatively recent development. I reviewed the diffuse-scattering data in uniform bulk semiconductor crystals analyzed with the help of kinematical diffraction theory. Only two types of defects, dislocation loops and spherical clusters, were found. The device consequences of the presence of these micro defects are yet to be established. For depth-dependent sample structures such as ion-implanted crystals or heterostructures, only experimental studies are available from a few authors. A practical theory of diffuse scattering for samples with a depth-dependent crystal structure or defect distribution still needs to be developed, and I introduced here a semikinematical diffraction formula that can be used to that end.

7. Summary

The double-crystal X-ray rocking-curve technique is an essential tool in the characterization of semiconductor structures. Its capability ranges from the relatively simple measurement of layer parameters including thickness, composition, strain, strain relaxation and structural quality, to the sophisticated analysis of heterostructure interfaces with submonolayer resolution and the evaluation of strained quantum-well layers. The 'fine-tuning' of the epitaxial growth technique may be feasible by using X-ray rocking-curve analysis as a 'quick' non-destructive characterization tool, to enable the growth of an optimum layer and interface structure for a specific device and circuit application.

An accurate determination of the layer and interface structural parameters depends greatly on the understanding of the physical principles involved in the HRXRD. Therefore, for the double-crystal and triple-crystal diffraction measurements, I have provided a discussion of some essential elements of the HRXRD techniques (Section 2); a summary review of some simple aspects for interpreting rocking curves (such as peak separation, FWHM, etc.) to determine the heteroepitaxial-layer parameters (Section 3); a summary of the dynamical and semikinematical X-ray diffraction theories for rocking-curve simulation, and description of a very useful correspondence between the kinematical diffraction of a monochromatic plane-wave X-ray (HRXRD) by a semiconductor heterostructure and the diffraction of a monochromatic plane-wave light (Fraunhofer diffraction) by a simple line grating (Section 4); a discussion of the physical principles and of the experimental/simulated X-ray rocking-curve data for interface analysis of heterostructures and for the layer analysis of strained quantum-well device structures (Section 5); and a review of the theory and the experimental

data in the diffuse X-ray scattering analysis of crystal defects in the Bragg geometry (Section 6).

It is hoped that this article contributes to the recognition by the semiconductor research and development community of the capability that the X-ray rocking-curve technique can provide in the analysis of heteroepitaxial interfaces.

The analysis of diffuse X-ray scattering is reasonably well established for bulk semiconductor crystals with a uniform defect distribution, since a practical theory is available. In this case, two types of defects, dislocation loops and spherical clusters of defects, were found by TCD and/or DCD diffuse-scattering analyses. However, for depth-dependent structures, there exists no practical theory for analysis of the diffuse X-ray scattering. An effort towards the development of such a theory is needed.

Acknowledgment

The work was supported in part by the US National Science Foundation under the grant numbers DMR-8857403 through the Presidential Young Investigator program and ECS-8913229.

References

[1] A. Segmuller, *Adv. X-ray Anal., 29* (1986) 353.
[2] B.K. Tanner, *J. Cryst. Growth, 99* (1990) 1315.
[3] B.M. Paine, *MRS Symp. Proc., 69* (1986) 39.
[4] U. Bonse and I. Hartmann, *Z. Kristall., 156* (1981) 265.
[5] T. Vreeland Jr., *J. Mater. Res., 1* (1986) 712.
[6] A. Fukuhara and Y. Takano, *Acta Cryst. A, 33* (1977) 137.
[7] J.F. Chen and C.R. Wie, *J. Electron. Mater., 17* (1988) 501; *J. Electron. Mater., 18* (1989) 399.
[8] R.N. Kyutt, P.V. Petrashen and L.M. Sorokin, *Phys. Status Sol. A, 60* (1980) 381.
[9] F. Cembali, M. Servidori, E. Gabilli and R. Lotti, *Phys. Stat. Sol. A, 87* (1985) 225.
[10] C.R. Wie, J.C. Chen, H.M. Kim, P.L. Liu, Y.W. Choi and D.M. Huang, *Appl. Phys. Lett., 55* (1989) 1774.
[11] C.R. Wie, *J. Appl. Phys., 65* (1989) 1036.
[12] R. Bhat, M.A. Koza, M.J.S.P. Brasil, R.E. Nahory, C.J. Palmstrom and B.J. Wilkens, *J. Cryst. Growth, 124* (1992) 576.
[13] S.J. Barnett, *J. Cryst. Growth, 103* (1990) 335.
[14] S. Ramesh, N. Kobayashi and Y. Horikoshi, *J. Cryst. Growth, 111* (1991) 752.
[15] P.H. Dederichs, *J. Phys. F, 3* (1973) 471.
[16] P.H. Dederichs, *Phys. Rev. B, 4* (1971) 1041.
[17] M.A. Krivoglaz, *Theory of X-Ray and Thermal Neutron Scattering by Real Crystals*, Plenum, New York, 1969.
[18] B.C. Larson and F.W. Young Jr., *Phys. Rev. B, 4* (1971) 1709.
[19] H. Trinkaus, *Phys. Status Sol. B, 51* (1972) 307.
[20] V. Holy and J. Kubena, *Phys. Stat. Sol. B, 170* (1992) 9.
[21] L.A. Charnity, A.N. Morozov, K.D. Scherbachov, V.T. Bublik and I.V. Stepantsova, *J. Cryst. Growth, 116* (1992) 369.
[22] P.F. Fewster, *J. Appl. Cryst., 25* (1992) 714; *Appl. Surf. Sci., 50* (1991) 9.
[23] V.S. Wang and R.J. Matyi, *J. Appl. Phys., 72* (1992) 5158.
[24] J.A. Ibers and W.C. Hamilton (eds.), *International Tables for X-ray Crystallography, Vol. IV*, Kynoch Press, Birmingham, UK, 1974, Sections 2.2 and 2.3.
[25] K. Nakayama, H. Hashizume, A. Miyoshi, S. Kikuta and K. Kohra, *Z. Naturforsch. B, 28a* (1973) 632.
[26] J.W.M. DuMond, *Phys. Rev., 52* (1937) 872.
[27] R.J. Matyi, *Rev. Sci. Instr., 63* (1992) 5591.
[28] W.H. Zachariasen, *Theory of X-ray Diffraction in Crystals*, Wiley, New York, 1945, pp. 116–119.
[29] I.K. Robinson, *Phys. Rev. B, 33* (1986) 3830.
[30] B.K. Tanner, A.G. Turnbull, C.R. Stanley, A.H. Kean and M. McElhinney, *Appl. Phys. Lett., 59* (1991) 2272.

[31] K. Kamigaki, H. Sakashita, H. Kato, M. Nakayama, N. Sano and H. Terauchi, *Appl. Phys. Lett., 49* (1986) 1071.
[32] J. Hornstra and W.J. Bartels, *J. Cryst. Growth, 44* (1978) 513.
[33] J.D. Wiley, in R.K. Willardson and A.C. Beer (eds.), *Semiconductors and Semimetals, Vol. 10*, Academic Press, New York, 1975.
[34] O. Madelung (ed.), *Semiconductors: Physics of Group IV Elements and III–V Compounds, Vol.17a*, Springer, New York, 1982.
[35] G. Simmons and H. Wang, *Single Crystal Elastic Constants and Calculated Aggregate Properties: A Handbook*, MIT Press, Cambridge, MA, 2nd edn., 1971.
[36] B.H. Lee, *J. Appl. Phys., 41* (1970) 2984.
[37] O. Madelung (ed.), *Semiconductors: Physics of II–VI and I–VII Compounds, Semimagnetic Semiconductors, Vol. 17b*, Springer-Verlag, New York, 1982.
[38] R.D. Greenough and S.B. Palmer, *J. Phys. D, 6* (1973) 587.
[39] P.F. Fewster and C.J. Curling, *J. Appl. Phys., 62* (1987) 415.
[40] C.R. Wie, *J. Appl. Phys., 66* (1989) 985.
[41] C.R. Wie and H.M. Kim, *J. Appl. Phys., 69* (1991) 6406.
[42] R.W. James, *The Optical Principles of The Diffraction of X-rays*, Ox Bow Press, Woodridge, CN, 1962.
[43] C.R. Wie, in P. Bhattacharya (ed.), *Properties of Lattice-Matched and Strained Indium Gallium Arsenide, EMIS Datareviews Series No. 8*, INSPEC, Institution of Electrical Engineers, London, 1993, p. 257.
[44] J. Lee, W.E. Mayo and T. Tsakalakos, *J. Electron. Mater., 21* (1992) 867.
[45] D.I. Westwood, D.A. Wolf and R.H. Williams, *J. Cryst. Growth, 98* (1989) 782.
[46] S. Fujita, Y. Nakaoka, T. Uemura, M. Tabuchi, S. Noda, Y. Takeda and A. Sasaki, *J. Cryst. Growth, 95* (1989) 224.
[47] D. Li, J.M. Gonsalves, N. Otsuka, J. Qui, M. Kobayashi and R.L. Gunshor, *Appl. Phys. Lett., 57* (1990) 449.
[48] Z.C. Huang and C.R. Wie, *Solid State Electron., 36* (1993) 767.
[49] Z.C. Huang, C.R. Wie, K. Evans, C.E. Stutz and D.A. Johnston, *J. Appl. Phys., 73* (1993) 4362.
[50] Y.-W. Choi, C.R. Wie, K.R. Evans and C.E. Stutz, *J. Appl. Phys., 68* (1990) 1303.
[51] Y.W. Choi, H.M. Kim, K. Xie and C.R. Wie, *J. Electr. Mater., 20* (1991) 545.
[52] J.W. Matthews and A.E. Blakeslee, *J. Cryst. Growth, 27* (1974) 118.
[53] R. People and J.C. Bean, *Appl. Phys. Lett., 47* (1985) 322.
[54] C.R. Wie, *J. Appl. Phys., 65* (1989) 2267.
[55] B.W. Dodson and J.Y. Tsao, *Appl. Phys. Lett., 51* (1987) 1325; *Appl. Phys. Lett., 52* (1988) 852(E).
[56] C.G. Darwin, *Phil. Mag., 27* (1914) 315,675.
[57] P.P. Ewald, *Ann. Phys. (Leipzig), 54* (1917) 519.
[58] J.A. Prins, *Z. Phys., 63* (1930) 477.
[59] S. Takagi, *Acta Cryst., 15* (1962) 1311.
[60] S. Takagi, *J. Phys. Soc. Jpn., 26* (1969) 1239.
[61] D. Taupin, *Bull. Soc. Franc. Miner. Cryst., 87* (1964) 469.
[62] W.J. Bartels and W. Nijman, *J. Cryst. Growth, 44* (1978) 518.
[63] A. Segmuller, P. Krishna and L. Esaki, *J. Appl. Cryst., 10* (1977) 1.
[64] V.S. Speriosu, *J. Appl. Phys., 52* (1981) 6094.
[65] F. Cembali, M. Servidori and A. Zani, *Solid-State Electron., 28* (1985) 933.
[66] V.S. Speriosu and T. Vreeland Jr., *J. Appl. Phys., 56* (1984) 1951.
[67] D. de Fontaine, *Metall. Soc. Conf., Vol. 36*, Gordon Breach, New York, 1966, p. 51.
[68] A. Segmuller and A.E. Blakeslee, *J. Appl. Cryst., 6* (1973) 19.
[69] H. Bohm, *Acta Cryst. A, 31* (1975) 622.
[70] B. Klar and F. Rustichelli, *Nuovo Cimento B, 13* (1973) 249.
[71] B.C. Larson and J.F. Barhorst, *J. Appl. Phys. 51* (1980) 3181.
[72] M.A.G. Halliwell, M.H. Lyons and M.J. Hill, *J. Cryst. Growth, 68* (1984) 523.
[73] M.J. Hill, B.K. Tanner, M.A.G. Halliwell and M.H. Lyons, *J. Appl. Cryst., 18* (1985) 446.
[74] C.R. Wie, T.A. Tombrello and T. Vreeland Jr., *J. Appl. Phys., 59* (1986) 3743; *J. Appl. Phys., 70* (1991) 2481(E).
[75] W.J. Bartels, J. Hornstra and D.J.W. Lobeek, *Acta Cryst. A, 42* (1986) 539.
[76] D.W. Berreman, *Phys. Rev. B, 14* (1976) 4313.
[77] A.T. Macrander, E.R. Minami and D.W. Berreman, *J. Appl. Phys., 60* (1986) 1364.
[78] N. Kato, *Acta Cryst. A, 47* (1991) 1.
[79] I.C. Bassignana and C.C. Tan, *J. Appl. Cryst., 22* (1989) 269.
[80] M. Born and E. Wolf, *Principles of Optics*, Pergamon Press, New York, 5th edn., 1975, p. 404.
[81] B.R. Bennett, B.V. Shanabrook, R.J. Wagner, J.L. Davis and J.R. Waterman, *Appl. Phys. Lett., 63* (1993) 949.
[82] G. Tuttle, H. Kroemer and J.H. English, *J. Appl. Phys., 67* (1990) 3032.
[83] D.H. Chow, R.H. Miles and A.T. Hunter, *J. Vac. Sci. Technol. B, 10* (1992) 888.
[84] J.R. Waterman, B.V. Shanabrook, R.J. Wagner, M.J. Yang, J.L. Davis and J.P. Omaggio, *Semicond. Sci. Technol., 8* (1993) S106.

[85] C. Giannini, L. Tapfer, E. Tournie, Y.H. Zhang and K.H. Ploog, *Appl. Phys. Lett., 62* (1993) 149.
[86] R.L. Gunshor, M. Kobayashi, N. Otsuka and A.V. Nurmikko, *J. Cryst. Growth, 115* (1991) 652.
[87] T. Baumbach, H.-G. Bruhl, H. Rhan and U. Pietsch, J. Appl. Cryst., 21 (1988) 386.
[88] S. Bensoussan, C. Malgrange and M. Sauvage-Simkin, *J. Appl. Cryst., 20* (1987) 222.
[89] J. Ouyang, Z. Mai, S. Cui, J. Li and C. Li, *J. Mater. Sci., 27* (1992) 6765.
[90] J.M. Vandenberg, A.T. Macrander, R.A. Hamm and M.B. Panish, *Phys. Rev. B, 44* (1991) 3991.
[91] S. Cockerton, S.J. Miles, G.S. Green and B.K. Tanner, *J. Cryst. Growth, 99* (1990) 1324.
[92] R. Meyer, M. Hollfelder, H. Hardtdegen, B. Lengeler and H. Luth, *J. Cryst. Growth, 124* (1992) 583.
[93] X.S. Jiang, A.R. Clawson and P.K.L. Yu, *J. Cryst. Growth, 124* (1992) 547.
[94] A. Antolini, P.J. Bradley, C. Cacciatore, D. Campi, L. Gastaldi, F. Genova, M. Iori, C. Lamberti, C. Papuzza and C. Rigo, *J. Electron. Mater., 21* (1992) 233.
[95] L. Pauling, *The Nature of the Chemical Bond*, Cornell University Press, New York, 1960, Chapter 4.
[96] J.C. Phillips, *Bonds and Bands in Semiconductors*, Academic Press, New York, 1973, p. 21.
[97] L. Tapfer, M. Ospelt and H. von Kanel, *J. Appl. Phys., 67* (1990) 1298.
[98] C.A. Wang, S.H. Groves, J.H. Reynolds and D.R. Calawa, *J. Electron. Mater., 22* (1993) 1365.
[99] C.R. Wie, unpublished data (1993).
[100] Y.W. Choi, H.M. Kim and C.R. Wie, *MRS Symp. Proc., 240* (1992) 627.
[101] C.R. Wie and Y.W. Choi, *Appl. Phys. Lett., 58* (1991) 1077.
[102] Y.W. Choi and C.R. Wie, *J. Appl. Phys., 71* (1992) 1853.
[103] D. Feketa, K.T. Chan, J.M. Ballantyne and L.F. Eastman, *Appl. Phys. Lett., 49* (1986) 1659.
[104] C.C. Eugster, *IEEE Electron Dev. Lett., EDL-12* (1991) 707.
[105] S.S. Lu and C.C. Huang, *IEEE Electron Dev. Lett., EDL-13* (1991) 214.
[106] H.M. Kim, *Ph.D. Dissertation*, State University of New York at Buffalo, 1992.
[107] H. Eckstein, *Phys. Rev., 68* (1945) 120.
[108] K. Huang, *Proc. R. Soc. Lond. A, 190* (1947) 102.
[109] H. Trinkaus, *Phys. Status Sol. B, 54* (1972) 209.
[110] B.C. Larson and F.W. Young Jr., *Z. Naturforsch. B, 28* (1973) 626.
[111] B.C. Larson and W. Schmatz, *Phys. Rev. B, 10* (1974) 2307.
[112] N. Kato, *Acta Cryst. A, 36* (1980) 763,770.
[113] V. Holy, *Phys. Stat. Sol. B, 11* (1982) 341.
[114] P.V. Petrashen, *Metallofizika, 8* (1976) 35.
[115] V.A. Buchuev, *Sov. Phys. Crystallogr., 34* (1989) 163.
[116] P. Zaumseil and U. Winter, *Phys. Stat. Sol. B, 120* (1990) 67.
[117] A. Iida and K. Kohra, *Phys. Stat. Sol. A, 51* (1979) 533.
[118] C.R. Wie, unpublished result (1993).
[119] P. Riglet, M. Sauvage, J.F. Petroff and Y. Epelboin, *Phil. Mag. A, 42* (1980) 339.
[120] I.R. Entin, V.I. Khrupa and L.I. Datsenko, *J. Appl. Cryst., 23* (1990) 355.
[121] E.L. Gartstein, *Z. Phys. B, 88* (1992) 327.
[122] A.N. Morozov and V.T. Bublik, *J. Cryst. Growth, 97* (1989) 475.
[123] A.A. Lomov, P. Zaumseil and U. Winter, *Acta Cryst. A, 41* (1985) 223.
[124] M.-F. Beaufort, *Nucl. Instr. Meth. B, 62* (1992) 478.
[125] L.A. Charnity, A.N. Morozov, V.T. Bublik, K.D. Scherbachev, I.V. Stepantsova and V.M. Kaganer, *J. Cryst. Growth, 118* (1992) 163.
[126] P. Franzosi, *J. Cryst. Growth, 126* (1993) 85.
[127] Z.H. Ming, A. Krol, Y.L. Soo, Y.H. Kao, J.S. Park and K.L. Wang, *Phys. Rev. B, 47* (1993) 16373.
[128] S.K. Sinha, E.B. Sirota, S. Garott and H.B. Stanley, *Phys. Rev. B, 38* (1988) 2297.
[129] S.K. Sinha, *Physica B, 173* (1991) 25.